International Journal of Hydrogen Energy 69 (2024) 586–607

Contents lists available at ScienceDirect

International Journal of Hydrogen Energy

journal homepage: www.elsevier.com/locate/he

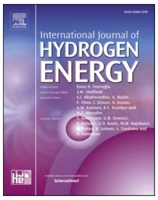

Experimental study and numerical simulation on porosity dependent direct reducibility of high-grade iron oxide pellets in hydrogen

Behzad Sadeghi [a,*], Pasquale Cavaliere [a,**], Mutlucan Bayat [a], Niloofar Ebrahimzadeh Esfahani [b,c], Aleksandra Laska [d], Damian Koszelow [e]

[a] Department of Innovation Engineering, University of Salento, Via per Arnesano, 73100, Lecce, Italy
[b] Faculty of Electrical Engineering and Information, Slovak University of Technology, Ilkovicova 3, 81219, Bratislava, Slovakia
[c] Omnics Research Group, Department of Mathematics and Physics University of Salento, CNR-Institute of Nanotechnology, INFN Sezione di Lecce, Via per Monteroni, 73100, Lecce, Italy
[d] Faculty of Mechanical Engineering and Ship Technology, Gdansk University of Technology, Narutowicza 11/12, 80- 233, Gdansk, Poland
[e] Advanced Materials Centre, Faculty of Electronics, Telecommunications and Informatics, Gdansk University of Technology, 80-233, Gdansk, Poland

ARTICLE INFO

Keywords:
Hydrogen-based direct reduction
Numerical
Simulation
High grade
Iron oxide pellets

ABSTRACT

The transition to more environmentally friendly steel production methods has intensified research into hydrogen-based direct reduction (HyDR) of iron oxide pellets. The aim of this study is to systematically investigate the kinetics of the reduction process, the evolution of porosity and the resulting microstructural changes on the reduction behavior of high-quality pellets during HyDR of iron ore at different temperatures. A modified mathematical model is developed based on the shrinkage kernel model, taking into account both mass and heat transport in a hydrogen atmosphere. The effects of temperature, particle size and time on the reduction behavior of the pellets are investigated. The simulated results are validated and discussed by the results of a batch of iron oxide pellets consisting of ten almost spherical pellets subjected to the direct reduction process with pure hydrogen. The results show that the total energy input to the HyDR process is a complex balance of factors, including chemical reaction rates, diffusion dynamics and entropy generation. The increase in free volume and simultaneous decrease in pore diameter reflect the dynamic nature of the microstructure, which includes additional free volume and defects due to the volume discrepancies and associated stresses between the reactant and product phases. Furthermore, the data show that higher temperatures accelerate the reduction reactions, especially the transformation of wustite into metallic iron. This phase transition is characterized by a significant volume change that cannot be accommodated by elastic deformation alone, leading to the development of lattice defects such as cracks, creep pores and dislocations that serve as stress relief mechanisms. The trends for porosity change at 950 °C and 1000 °C observed in the experimental results are correct and in good agreement with the numerical and simulated results.

1. Introduction

Iron production is a crucial step in the manufacture of iron and steel. It involves the conversion of iron ore into molten iron through a series of chemical reactions. The current annual consumption of iron ore for this process amounts to 2.3 billion tons, from which about 1.32 billion tons of pig iron are extracted [1–3]. This concern is a top priority for the industry, as more than 70% of the world's iron production currently takes place via a blast furnace and a downstream oxygen converter [4]. In reality, such a large amount of CO_2 production contradicts the goals of achieving low-carbon steel production and reducing CO_2emissions by over 80% by 2050 [5–7]. An alternative approach to large-scale and sustainable iron oxide reduction is hydrogen-based direct reduction (HyDR) of iron oxide, which is attracting a lot of attention in the iron and steel industry as one of the most promising solutions in this context [4,8,9]. The most common burden materials were used for the direct-reduced iron (DRI) process, are pellets that generally containing pre-porosities with different size and the surface area.

The process of iron production is essentially complex and involves various stages, each of which has its own characteristics and

---

* Corresponding author.
** Corresponding author.
E-mail addresses: behzad.sadeghi@unisalento.it (B. Sadeghi), pasquale.cavaliere@unisalento.it (P. Cavaliere).

https://doi.org/10.1016/j.ijhydene.2024.05.050
Received 15 March 2024; Received in revised form 18 April 2024; Accepted 4 May 2024

requirements. An important aspect of iron production is the porosity of the starting material, such as iron oxide ore and pellets. Porosity, i.e. the presence of open spaces or voids in the material, plays an important role in determining the efficiency and quality of the ironmaking process. Iron ore pellets, on the other hand, are a manufactured product that is used as a feedstock for iron production. Pellets are produced in the pelletizing process by agglomerating fine iron ore particles into small, spherical balls, which inevitably creates porosity [10,11]. In the context of ironmaking, porosity refers to the presence of voids or pores in the feedstock materials, such as iron oxide ore and pellets. Porous pellets allow for better gas–solid reduction behavior, which promotes the transport of heat and mass during ironmaking reactions [12].

This leads to faster reaction rates and improved overall process efficiency. In addition, the porosity of the iron oxide pellets has an effect on the mechanical strength of the materials, which is important for handling and transportation. Porosity plays a crucial role in direct reduction as it has a direct impact on the efficiency and productivity of the process, i.e. on the reduction rate, the gas-solid reactions and the gas transport within the reactor [11,13]. In gas–solid reduction reactions, high porosity facilitates the diffusion of gas molecules and further promotes the reduction reactions [12]. In other words, the reduction time correlates with the absolute porosity and the size of the surface pores. Larger pores lead to a faster reduction, depending on the density of the pellet, with a higher density leading to a longer reduction time [14,15]. In this context, previous literature has documented that the microstructural elements and the impurities dissolved in the pellets can have significant effects on the HyDR behavior of iron oxide pellets and influence the microstructural changes during reduction, the pore size distribution and the overall reduction kinetics [14,16,17]. Cavaliere et al. [14,15,18], studied the hydrogen direct reduction and processing parameters on the reduction behavior of high-quality pellets and showed a remarkable increase in porosity when the pellets are fully metallized. They also showed that the pore size and the tortuosity of the pores increase as the hydrogen reduction progresses. The presence of various impurities and intermediate iron oxide variants can also influence the nano/microstructure and chemistry of the resulting iron, which can affect its properties and quality [17].

In an industrial reactor for the DR process, the movement of the oxide pellets leads to changes in the chemical potentials of the gaseous species and the temperature. These fluctuations are caused by the interaction between the pellets and the injected gas mixture. In addition, the chemical potentials of the species within the individual pellets can differ at a certain position [19]. These variations can be caused by factors such as the composition and structure of the pellet itself as well as the local conditions in the reactor. It is therefore necessary to understand these variations in chemical potentials. Temperature is critical for optimizing reactor performance and ensuring efficient processing of the oxide pellets. In addition, the process of reducing the pellets with gasses involves three main phases [2,19]. In the gas phase, a mass transfer takes place first, i.e. the movement of the gasses within the reactor. This interaction between the gas mixture and the sintered pellets facilitates the efficient transfer of reactants and products, and the effectiveness of this mass transfer is critical to the overall reduction reaction. Once the gasses have come into contact with the sintered pellets, they must flow through the product layer surrounding the pellets. This layer, which consists of reaction products from the reduction process, requires efficient mass transfer so that the reactants can reach the oxide interface for the subsequent chemical reactions. The chemical reactions that make up the reduction reaction ultimately take place at the interface between the product layer and the oxide pellets. Factors such as temperature and time of reduction, gas composition and the properties of the pellets influence these reactions. To achieve a successful reduction of sintered pellets by gasses, it is crucial to understand and optimize these main steps. To fully understand the behavior of pellet reduction and to enable efficient dynamic control, it is therefore essential to develop an accurate mathematical model that describes the intrinsic properties of the pellet.

There is modeling work for the reduction of single pellets by different mechanisms and for multi-particle reduction processes [20–28]. In general, three primary mathematical models have been used to model pellet reduction: the non-reacting shrinking core model with one interface, the non-reacting shrinking core model with three interfaces, and the porous solid model (also known as the grain model). In a paper by Bonalde et al. [28], the grain model describes the reduction kinetics of iron ore pellets. The model with an interface was a fundamental mathematical model based on the chemical reaction of iron and wustite (W) at the interface and incorporated Fick’s law to determine the mass transfer of gas species within the pellet [29,30]. The behavior of gas transfer in the porosities as a control step of the overall reduction process was described according to the previously published literature. The investigation of the influence of pellet diameter and porosity on the reduction showed that increasing the porosity accelerates the diffusion of the gas species, which leads to a faster reduction process [14,31]. In addition, the size of the pores decreases from the larger pellet to the middle one, only to increase again in the pellet with the smallest diameter [10]. On the one hand, the differences in the physical and chemical properties of iron ore pellets and, on the other hand, the kinetic parameters such as time and temperature considerably limit the applicability of existing process models to different types of pellets and experimental conditions. Therefore, a mathematical model that takes into account the exact structural details of the pellet for the direct reduction of iron oxide pellets must include the type of physical properties, reduction time and local temperature. The current approach provides a solid basis for dynamic modeling of the pellet reduction process, but further efforts are certainly needed to create a realistic process model.

Considering the different steps involved in the reduction of pellets by gasses, the development of a process model requires a careful identification of the reduction mechanisms. To develop an effective process model, it is critical to examine the intricacies of the individual steps and how they interact. By carefully identifying and characterizing the reduction mechanisms and the gas behavior in the pre-porosities, the process model can accurately represent the complex dynamics of the reduction process. In addition, the process model should take into account the variations in temperature, time and the properties of the oxide material. These factors significantly influence the reduction mechanisms and must be included in the model to ensure its accuracy and reliability. The development of a process model that takes into account the different steps in the reduction of sintered pellets by gasses therefore requires a comprehensive understanding of the underlying mechanisms.

Besides all the advantages that the developed models have in the field of direct reduction of iron ore pellets, the lack of consideration of the initial geometry of the starting pellet, which can lead to various non-uniformities in terms of temperature distribution, the behavior of the gas in the pores as well as the active mass transfer of the materials during the reduction process, can be mentioned as the most important obstacle and dilemma of these models. In this context, Qiu et al. [29,30] have recently shown that the gas behavior in terms of velocity and pressure within the pores of a pellet can be anisotropic and strongly depends on the properties of the pores. In this context, this article aims to investigate the crucial role of porosity on the reducibility behavior of iron oxide rock through a combined approach based on experimental data and numerical simulations of a real porous pellet based on X-ray computed tomography images. The development and evolution of both qualitative and quantitative porosity and the effective role of this parameter on the mechanisms involved in the process of direct reduction of iron ore pellets are closely monitored and discussed in detail. In the present study, a modified mathematical model is developed based on the model of the shrinkage core, taking into account both mass and heat transport in a hydrogen atmosphere. The effects of temperature, particle size, time and porosity on the reduction behavior of pellets are investigated. The simulated results are validated and discussed using the results of a batch of iron oxide pellets consisting of 10 nearly spherical pellets subjected to the direct reduction process with pure hydrogen. In the present work, the high-level pellet tomography images were simulated with the finite element method (FEM) using COMSOL Multiphysics software to obtain detailed insights into the complex physical phenomena governing the process, including porosity coalescence caused by the reduction, gas flow and heat transfer within the pellets, reaction kinetics and gas-solid interactions.

2. Experimental section

Reduction experiments were carried out with the pellet samples provided by VALE (Brazil). The main mineral phase of the pellet was hematite, Fe_2O_3, (H) and a small amount of magnetite, Fe_3O_4, (M) and quartz, as indicated in Table 1.

The pellets analyzed in the present study were provided by VALE (Brazil); the production process of the pellets is described in detail in Ref. [14]. The selected pellets had a good spherical shape with an average diameter in the range of 1–2 cm (Fig. 1(a)), a density of 3600–5200 kg/m^3 and a specific surface area of 1500–1600 cm^2/g. The density of the pellets was determined by measuring seven diameters of the pellets. After calculating the average diameter of the pellets, these were used to calculate the density after the pellets were weighed with a precision balance. The pellet reduction experiments were carried out in a self-designed and developed shaft furnace (Fig. 1(b)).

The experiments on direct reduction were carried out in the temperature range 950–1000 °C. The gas composition was high-purity hydrogen (99.99 pct) at pressures of 1–8 bar. The flow rate of the reducing gas was 0.5 L/min and the basicity index (referred to as CaO/SiO_2 ratio) was between 0 and 2.15. Pure hydrogen was used to isolate its effects on reducibility and microstructural changes, eliminating variables from impurities. This selection acts as a standard for future comparisons. The flow rate of 0.5 L/min, chosen based on initial tests and literature [32,33] ensures thorough reduction and aligns with industrial practices for applicability. Three tests were performed for each condition to ensure reproducibility of the results. The pore aspect and the evolution of the pellet were analyzed by microtomography using Phoenix v/tome/x s (General Electric). X-ray computed microtomography is a non-destructive technique that allows the internal and three-dimensional visualization of a sample exposed to ionizing radiation without the need for physical or chemical preparation of the pellet. It is based on the same principles as conventional radiography, in which each part of a sample absorbs the rays differently. In this way, it is possible to examine two-dimensional cross-sections non-destructively and reconstruct them through mathematical principles to create the corresponding three-dimensional model of the sample, which allows the visualization and quantification of the internal structure of the material. Computed tomography produces an image that is very close to reality by displaying the average attenuation of each small-volume element, organizing the beam attenuation information and quantifying the information [14,34,35]. The segmentation of the pores was performed with the free software FIJI/ImageJ. A lower limit was set visually, where some pores were not selected, and an upper limit, where pores that were not yet filled could be selected. The threshold (maximum or minimum) was set for all sample layers. The determination of the threshold value is important as it has a significant influence on the determination of the porosity percentage of iron ore pellets [14]. The degree of reduction, R_{ex}, is defined by Ref. [19] as follows,

$$R_{ex} = \frac{W_0 - W_t}{W_0 - W_\propto}$$

Where W_0, W_t and $W_\propto$ are the initial weight of the pellet, the weight of the pellet at time t, and the theoretical weight after complete reduction, respectively. The details of the experiment have been described in previous publications by our group [10,14,36]. Since the kinetics of the direct reduction process is directly influenced by the properties of the reducing gas (temperature, pressure and type of gas), the temperature and time of reduction and the physical properties of the pellet (diameter, density, porosity and tortuosity), there are two different modes. In this context, a HyDR process for pellets is considered. In the first case, we only considered the temperature and time changes in the evolution of porosity and tortuosity (unreduced state). In the second case, the role of the reducing gas on the evolution of porosity and tortuosity was investigated at the same temperature and time as before (reduced state).

3. Numerical approach

Numerical modeling of the reduction processes plays a central role in deciphering the complex transformation of H into iron, which involves a sequence of reactions: H (H) → M (M) → Wustite (W) → Iron (Fe).

In this section, a model is presented that focuses on the evolution of the physical properties of the pellets during the DRI process (Fig. 2). It was specifically developed to decipher the intricate interplay of parameters that control the reducibility of H pellets. Of greatest importance are the dynamic changes in the evolution of porosity and tortuosity during the reduction phases, which influence the course of the individual reactions. In this context, reducibility is an important parameter that quantifies the degree of conversion of H to iron during the reduction reactions. In the following sections, we focus on the detailed structure of our model and emphasize the indispensable role of porosity evolution and changes in tortuosity. This paper deals with the meaning of the individual terms, explains the reasons for the choice of parameters and their respective exponents, and highlights the complicated dynamics of the HyDR process.

Studies have shown that porosity and pore size develop as a function of the reduction temperature, which underlines their importance for the process [10]. In contrast, tortuosity, which characterizes the path of particles through a medium, is also a decisive factor [14,18]. The relationship between porosity, tortuosity and permeability is of fundamental importance because tortuosity influences the flow behavior through porous media and thus affects the overall efficiency of the direct reduction process. Therefore, understanding and quantifying the importance of porosity and tortuosity is essential for optimizing the direct reduction process and predicting the behavior of iron oxide pellets during the direct reduction process. To better understand how porosity and tortuosity evolve during the direct reduction process, it is necessary to investigate the influence of temperature and time on these factors prior to HyDR.

The reduction of Fe2O3 does not occur directly to metallic Fe. If the reduction temperature is below 570 °C, the reduction to Fe occurs gradually from Fe2O3 to Fe3O4 and further to Fe. At reduction temperatures of more than 570 °C, on the other hand, the reduction takes place from Fe2O3 via Fe3O4 to Fe(1-x)O and then on to Fe. In the simplest and most widely accepted model in the literature [37–39], the HyDR process is characterized by a hierarchy of phenomena that can influence the reaction at different lengths and time scales [14,40], as shown in Fig. 3. This process begins with a chemical reaction on the outer surface of the pellet with hydrogen gas and continues with the diffusion of hydrogen into the porous iron layer that develops towards the interior of the pellet to reach the interface between Fe and Fe(1-x)O

Table 1
The chemical compositions of the pellets (all values are in wt. Percent).

TFe (%)	Fe_2O_3%	CaO (%)	Mn (%)	Al_2O_3 (%)	SiO_2 (%)	P (%)	MgO (%)	S (%)
67.24	96.63	1.02	0.144	0.38	1.97	0.031	0.63	0.018

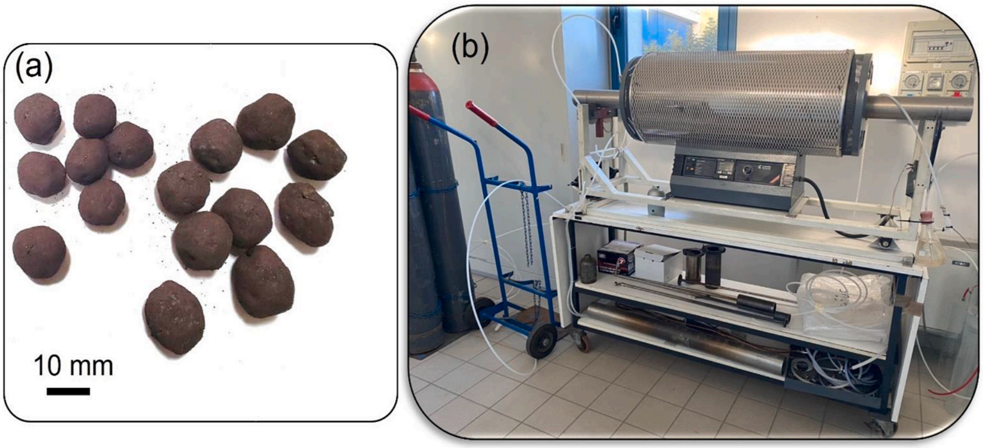

Fig. 1. (a) Pellets employed in the present study (b) Self-designed shaft furnace.

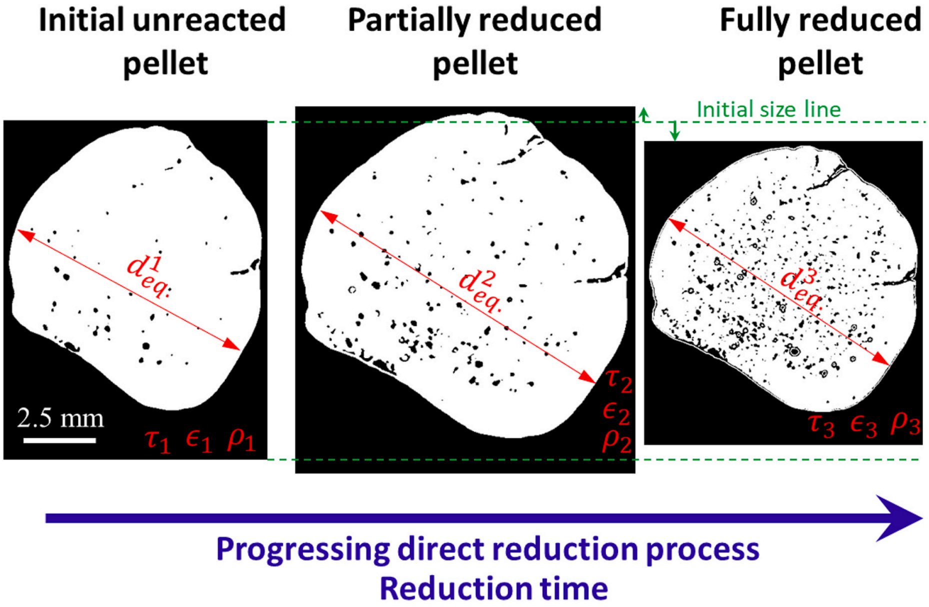

Fig. 2. Reaction process in progressive conversion mode based on shrinking core/particle model. $d_{ed.}$, τ, ϵ, and ρ are the equivalent diameter, tortuosity, porosity and density of pellet. The green dashed line indicates the change in diameter in at least one direction. (For interpretation of the references to color in this figure legend, the reader is referred to the Web version of this article.)

and produce iron and water. The part of the gas that is on its way to the center of the pellet diffuses into the Fe(1-x)O layer to reach the Fe(1-x)O/Fe3O4 interface, which in turn causes the reduction of M to Fe(1-x)O. Finally, the remaining hydrogen gas diffuses into the M layer to reach the M-M interface. In this step, H is reduced to M to complete the reduction reaction. It can be concluded that various phase transformations, mass transfer and mechanical interactions take place throughout the process, which together lead to the development of the reduction process.

The pellet mesh is shown in Fig. 4, which contains between 170,000 and 200,000 (plus 55000–60000 internal degrees of freedom) triangular cells for different geometries. Direct reduction with hydrogen reveals complex physico-chemical-mechanical interactions leading to very complex reduction mechanisms characterized by continuous steps in terms of mass transport and volume changes. Chemical non-catalytic solid-gas reactions involve heat transfer, mass transfer, chemical reactions, changes in physical properties, etc [40–42]. In other words, the reduction of pellets by a gas must take place in the following process steps: Mass transfer in the gas phase, mass transfer within the solid product layer, chemical reaction between the reducing agent and the solid oxide, formation of water vapor and carbon dioxide, iron oxides and iron, diffusion of the reaction products in the solid state and diffusion of the gaseous products back to the pellet surface [15,30]. This dynamic behavior leads to complications in the precise analytical analysis of the entire reduction process. The main hypotheses proposed to simplify the process are therefore as follows.

- Both the gas and solid phases are considered continuous, and the gas phase obeys the ideal gas law.
- The density of the gas is constant
- The reactions are reversible: first-order and proceed topochemically.

4. Reduction kinetic

4.1. Evolution of pellet porosity and tortuosity

Porosity and tortuosity are crucial parameters in the HyDR process that significantly influence the performance and properties of iron oxide

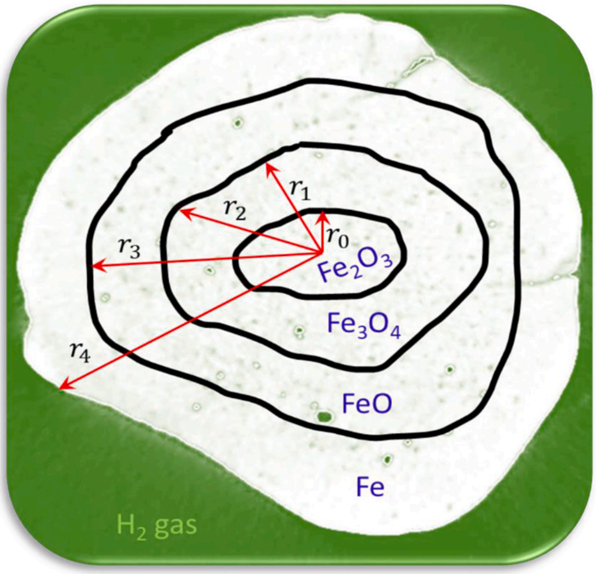

Fig. 3. The three-layer model of the unreacted shrinking core shows the product layers Fe3O4, FeO, and Fe as well as the H core Fe2O3. Each particle was surrounded by an atmosphere of H_2-gas.

pellets. Porosity plays a crucial role in facilitating gas penetration, increasing reaction rate and improving reduction performance. It influences gas diffusion, permeability and overall reduction kinetics by providing pathways for efficient gas flow and reaction sites. Conversely, tortuosity has a negative effect on gas diffusion, leading to slower rates and lower efficiency due to longer path lengths and obstacles. It also affects permeability, hinders gas flow and causes uneven distribution within the pellet structure, leading to localized reactions and lower rates. Overall, both porosity and tortuosity influence the effective utilization of the reduction gas and thus determine the success of the reduction process.

4.2. Unreduced state

Time and temperature play an important role in the palletization and direct reduction of iron oxide pellets. In connection with palletizing, temperature and time have a considerable influence on the physical and chemical transformations of the iron ore particles. Studies [14,18,36,43–45] have shown that the reduction temperature has a considerable influence on the extent of reduction in the direct reduction of iron oxide pellets. The temperature profiles and the temperature within the particles during the reduction process show the dynamic characteristics of temperature changes, which directly affect the reduction kinetics and the development of the pellet microstructure.

According to the literature [43,46,47], in palletization process the porosity rate $\left(\frac{d\varnothing}{dt}\right)_{Pel.}$ can be expressed as

$$\left(\frac{d\varnothing}{dt}\right)_{Pel.} = \mathrm{k} \times \varnothing^{n} \times \mathrm{e}^{(E/T)} \times \mathrm{t}^{m} \times \frac{1}{\tau^{p}} \times \frac{1}{\tau^{q}} \tag{1}$$

Where k, n, m, p, and q are the rate constants for the palletization process, an empirical constant related to the influence of porosity on the

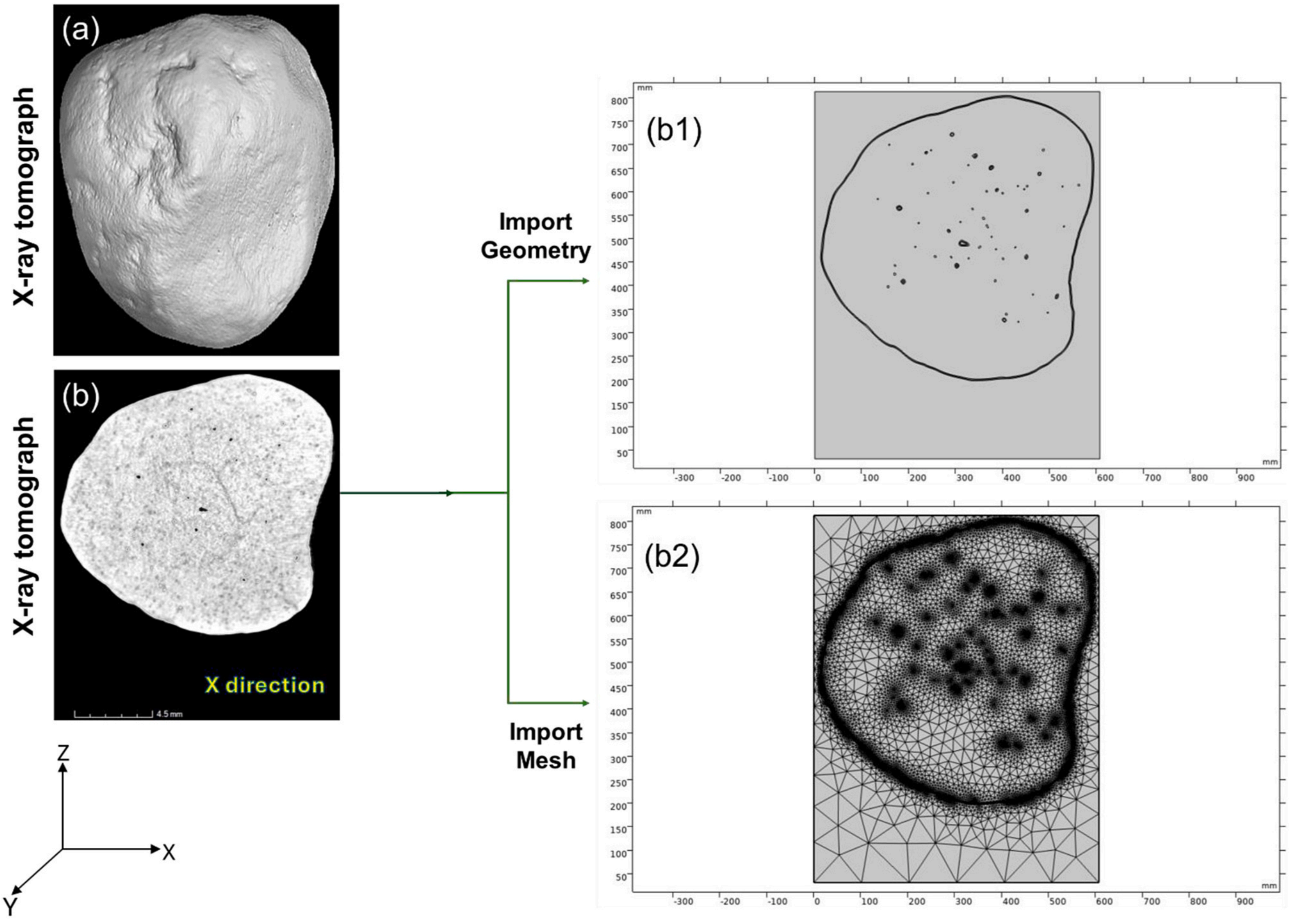

Fig. 4. Image processing steps: (a) original X-ray tomography image, (b) cross-sectional view with internal porosity in the X-direction, (b1) imported geometry, and (b2) corresponding tetrahedral meshing.

porosity rate, and an empirical constant related to the influence of time on the porosity rate, and empirical constant related to the influence of tortuosity on the porosity rate, respectively. ∅ and τ are the percentage of porosity and the tortuosity, while $\dot{\tau}$ is the tortuosity rate calculated from the derivative of the tortuosity with respect to time (Table 1S). E is the activation energy (~477,*kJ-mol.* [14]) and R is the gas constant (8.314,*J-mol.K.*). T is the temperature in Kelvin, and t is the time. All of these constants can be determined by nonlinear fitting in MATLAB using our experimental or simulation data. Table 2 lists the calculated values of all constants.

In order to calculate the porosity (∅) is calculated by

$$\varnothing = \frac{V_p}{V_{cell}} \tag{2}$$

Where V_p and V_{cell} are the pore volume and the total volume of the pellet, respectively. Tortuosity is the actual path length (L) through a porous medium with a straight-line or Euclidean distance ($L_{Eu.}$) that would be traveled in the absence of obstacles [48]. In addition, to calculate the tortuosity value, the X-ray computed tomography images were first binarized, and then the tortuosity was calculated based on the GR algorithm in the Fiji-ImageJ software. In addition, the porosity of a particle is defined as the ratio between the pore volume and the particle volume, and radius of a sphere with the same volume as the irregular object [30]. The calculated porosity values are the average porosity values in the X, Y, and Z sections based on the values obtained from the Gaussian fit of the porosity-size-frequency diagram generated using the Fiji-ImageJ software. It is worth noting that the porosity and tortuosity factors are specific characteristics of each type of pellet and are independent of the gas properties.

4.3. Reduced state

The pores in an iron ore depend on the duration of the reduction reaction, so that intermediate pores can form during the gradual reduction of iron ore. Moreover, the surface of the particles is usually not smooth and continuous but rough, and the particles may have internal cracks and become porous. In addition, in most pellets used as porous media, pores with different diameters are twisted and interconnected, and the path for diffusion of gas molecules within the pores is tortuous. Therefore, a transport mechanism considering all kinds of transport modes such as molecular diffusion, and Knudsen diffusion can be calculated by a D_i^{eff} for each gaseous species considering the total effective intraparticle diffusion as follows [49]:

$$D_{eff} = \frac{\varnothing}{\tau} D_i \tag{3}$$

In fact, $\frac{\varnothing}{\tau}$ is known as a porous media factor.

D_i can be expressed as follows:

$$\frac{1}{D_i} \cong \frac{1}{\mathrm{D_{iK}}} + \frac{1}{\mathrm{D_{ij}}} \tag{4}$$

Where D_{ij} and D_{iK} are the coefficient of molecular diffusion and Knudsen diffusion, respectively.

The D_{iK} is considered depending on the pore diameter of the porous pellet, measured in m^2/s and it can be calculated as

$$\mathrm{D_{iK}} = 1.054\ .\ \mathrm{d_p}\ .\ \sqrt{\frac{8\mathrm{RT}}{\pi \mathrm{M_i}}} \tag{5}$$

Where d_p, and M_i are the mean pore size of the porous media and the molecular weight of H_2 gas. Temperature (T) has units of K, and R is gas universal constant (8.314 J/mol.K).

Table 2
The constants calculated using Eq. (1).

k	n	m	p	q
6.98	−0.29 ± 0.08	−0.95 ± 0.11	0.0091 ± 0.001	0.0054 ± 0.006

Binary molecular diffusion (D_{ij}) is determined by the Fuller-Schettler-Giddings (FSG) correlation and can be defined as in [39,50]

$$\mathrm{D_{ij}} = \frac{0.00143.\ \mathrm{T}^{1.75}}{\mathrm{P_b}.\mathrm{MW}_{\mathrm{ij}}^{1/2}.\left(\left(\mathrm{V}_{\mathrm{i}}^{\frac{1}{3}} + \mathrm{V}_{\mathrm{j}}^{\frac{1}{3}}\right)\right)^2} \tag{6}$$

$$\mathrm{MW_{ij}} = \left[\frac{1}{\mathrm{MW_i}} + \frac{1}{\mathrm{MW_j}}\right]^{-1} \tag{7}$$

Where P_b (1 and 5 bar), MW_{H2} (~ 2 g/mol), MW_{H2O} (18 g/mol), V_{H2} (7.07 cm^3/mol [51]), and V_{H2O} (12.7 cm3/mol [51]) are the pressure, the molecular weight of H_2 and H_2O, and the diffusion volume of H_2 and H_2O, respectively. From binarized images and calculating the frequency diagram and the size distribution of the pores, the different equivalent radii of the pores within the pellet contain three categories namely, 1–7 μm(average ~ 4 μm, this average value was taken from small pellets reduced at 950 and 1000 °*C*), 8–20 μm (average ~ 14 μm, this average value was taken from medium pellets reduced at 950 and 1000 °*C*), and 21–50 μm (average ~ 36.72 μm, this average value was taken from big pellets reduced at 950 and 1000 °*C*). The values for the D_{ij} and D_{iK} are calculated based on the relevant equations and given in Table 3.

Table 4 shows the calculated effective diffusion coefficients for each pellet during HyDR. It should be noted that the values of ∅ and **τ** were calculated for different situations and given in Table 2S.

All images extracted from the Fiji ImageJ software can be found in the supplementary material. Relating porosity, the rate of porosity evolution ($\frac{d\varnothing}{dt}$) and tortuosity (τ) directly can be challenging, as these parameters depend on various factors and their relationships can be complex. Consider these basic concepts, such as 1- as porosity increases, tortuosity tends to increase as there are more pathways for diffusion, making the overall pathway more tortuous; 2- the rate of porosity development can indirectly affect tortuosity. If porosity develops rapidly, it could affect the overall structure and tortuosity.

The total porosity rate is made up of three hierarchical porosity rates, namely $\left(\frac{d\varnothing}{dt}\right)_{H\rightarrow M}$, $\left(\frac{d\varnothing}{dt}\right)_{M\rightarrow W}$, and $\left(\frac{d\varnothing}{dt}\right)_{W\rightarrow Fe}$.

$$\frac{d\varnothing}{dt} = \left(\frac{d\varnothing}{dt}\right)_{H\rightarrow M} + \left(\frac{d\varnothing}{dt}\right)_{M\rightarrow W} + \left(\frac{d\varnothing}{dt}\right)_{W\rightarrow Fe} \tag{8}$$

According to the modified volume reaction model developed by Ghalandari et al. [52],

$$\frac{d\varnothing}{dt} = 1 \bigg/ V_p\rho_p\left(R_{H\rightarrow M} + R_{M\rightarrow W} + R_{W\rightarrow Fe}\right) \tag{9}$$

Where V_p, and ρ_p are the initial density and initial pellet volume.

Taking into account the changing density in each layer, the effective diffusion coefficient of the porous particle was determined by considering the morphology of the particle, which in turn influenced the

Table 3
Coefficient values of molecular diffusion and Knudsen diffusion as a function of pore size at 1 bar pressure.

		950 °*C*	1000 °*C*
***D**$_{ij}$* **(*m*^{2}/*s*)**		14.90	15.99
***D**$_{iK}$* **(*m*^{2}/*s*)**	small	~479 × 10^{-6}	~489 × 10^{-6}
	medium	~1679 × 10^{-6}	~1713 × 10^{-6}
	big	~4404 × 10^{-6}	~ 4493 × 10^{-6}
D_i^t	small	~ 14.45 × 10^{-6}	~15.48 × 10^{-6}
	medium	~14.76 × 10^{-6}	~15.84 × 10^{-6}
	big	~14.84 × 10^{-6}	~15.93 × 10^{-6}

Table 4
The **effective total diffusion coefficient** ($cm^2.s^{-1}$) as function of pellet size at 950 °C and 1000 °C.

Pellet	950	1000
small	9.69×10^{-3}	5.53×10^{-3}
medium	9.77×10^{-3}	8.85×10^{-5}
big	1.52×10^{-5}	5.77×10^{-5}

density. Therefore, considering the density changes for each phase and the tortuosity, equation (8) can be rearranged as follows:

$$\frac{d\varnothing}{dt} = \left(\frac{M_H R_{H\to M}}{V_{p,H}\rho_{eff.,H}} + \frac{M_M R_{M\to W}}{V_{p,M}\rho_{eff.,M}} + \frac{M_W R_{W\to Fe}}{V_{p,W}\rho_{eff.,W}}\right) \tag{10}$$

Where the ρ_{eff} and V_p the effective density and pore volume. $R_{H\to M}$, $R_{M\to W}$, and $R_{W\to Fe}$ are the reaction rate of H to M, M to wustite, and wustite to iron, respectively.

In addition, the effective density of the H ($\rho_{eff.,H}$) can be defined as

$$\rho_{eff.,H} = (1 - \varnothing)\rho_{pure,H} \tag{11}$$

Where $\rho_{perfect,H}$ is the perfect particle density of the pellet wthout voids. The approximate pure densities (ρ_{pure}) of iron oxides are as follows: Fe_2O_3 or H has a density of approximately 5.24 g/cm^3, Fe_3O_4 or M has a density of approximately 5.17 g/cm^3, and FeO or wustite has a density of approximately 5.70 g/cm^3. The other product layers are also determined by the effective density of the reactant layer multiplied by the mass equivalent as follows:

$$\rho_{eff.,M} = \rho_{eff.,H}\; q_{m,H} \tag{12}$$

$$\rho_{eff.,W} = \rho_{eff.,M}\; q_{m,M} \tag{13}$$

Here $q_{C,A}$ stands for the mass equivalence which represents the mass of the product C for every consumption of A [37]. Knowledge of this point is necessary because diffusion is a key mechanism for the transport of species through interconnected pores during the sintering of porous materials. By defining the D_i^{eff} which takes into account different factors such as porosity, tortuosity and different diffusion modes, it is possible to correlate the mass transport and the evolution of porosity during the HyDR process. By introducing the effective diffusion coefficient into the porosity rate equation, it is assumed that the rate of porosity change is influenced by diffusion phenomena in porous media. The justification for this approach lies in the idea that the change in porosity over time is influenced by these diffusion characteristics, as the diffusion of species through the porous medium becomes more complicated due to factors such as porosity and tortuosity. Therefore, the D_i^{eff} can be included in eq. (10);

$$\frac{d\varnothing}{dt} = \left(\frac{M_H R_{H\to M}}{V_{p,H}\rho_{eff.,H}} + \frac{M_M R_{M\to W}}{V_{p,M}\rho_{eff.,M}} + \frac{M_W R_{W\to Fe}}{V_{p,W}\rho_{eff.,W}}\right).\, D_{eff} \tag{14}$$

It is worth noting that the values of density changes for different phases at different temperatures are on the order of micron scale, which is the reason why the density values are in more than five decimal places.

Considering the molecular weights (M) of Fe_2O_3:159.69 g/mol, Fe_3O_4:231.535 g/mol, and FeO: 71.845 g/mol, the porosity rate can be estimated by eq. (9). The rate of each reaction was estimated from the experimental results. Fig. 3 shows the reduction degree of reduction and the rate of reduction as a function of time at 950 °C and 1000 °C. Based on the experimentally observed reduction kinetics in terms of the reduction degree for the HyDR of commercial H pellets [2] and the HSC estimates for the evolution of the kinetic behavior and the reduced equilibrium amount [53,54], it can be concluded that the reduction rates of the first two average reduction rates, i.e. Fe2O3 to Fe3O4 and Fe3O4 to FeO, are extremely high, while they become much slower for the reduction of FeO to Fe [1]. It should be noted that most of the proposed models and experimental data have shown that the time required for the first, second, and third reactions is closely correlated with the pellet size, temperature, and other parameters. Therefore, based on the experimental and modeled results [1,2,19,30], the time required (Δt) required for the reduction of Fe2O3 to Fe3O4, followed by the reduction of Fe3O4 to FeO, and finally, the reduction of FeO to Fe is estimated differently for each intermediate reaction and pellet size in this work. According to our database and preliminary experimental results, the maximum times required for the reduction of Fe2O3 to Fe3O4, Fe3O4 to FeO, and FeO to Fe are approximately 2–5 min, 5–30 min, and 30–90 min, respectively.

In addition, the HyDR process is known as a hierarchy of phenomena that can influence various reactions from transport and reaction kinetics to chemical reactions that occur on different length and time scales. It is therefore to be expected that changes can be observed in the curve of reaction rate versus time (Fig. 5), which can be explained by the kinetic and thermodynamic differences of the reactions [2,11,55,56]. However, due to the strong dependence of the reaction rate on temperature, the regions related to the individual phase partially overlap at higher reduction temperatures. Therefore, in this study, an attempt was made to estimate the average reaction rate for each intermediate reaction using the plots shown in Fig. 6. It shows the dependence of the reaction rate on the degree of reduction and time for different sizes of H pellets at 950 °C and 1000 °C. The calculated values are given in Table 5.

Figs. 7–9 show microtomographic images of small, medium and large pellets, respectively, showing their pore aspects and development in both unreduced and reduced states after exposure to HyDR at 950 °C for 90 min. Fig. 7(a) shows that the surface appears relatively smooth with only minor irregularities. The cross-sections shown in Fig. 7(a1, a2 and a3) illustrate the internal microstructure in different directions. The porosity is visible as dark spots within the material. The distribution of the pores appears to be relatively uniform in the different directions, with no significant orientation or alignment of the porosity. As can be seen in Fig. 7(b), there was a visible crack on the surface, suggesting that the reaction induced stresses within the pellet that led to fracture. The cross-sections shown in Fig. 7(b1), (b2) and (b3) reveal changes in the internal microstructure after the reaction. The pores appear to be larger and show an increased tendency to coalesce, especially in Fig. 7(b1) and (b2).

Fig. 8 shows the microtomographic images of a medium-sized pellet, comparing the microstructures during direct reduction at 950 °C for 90

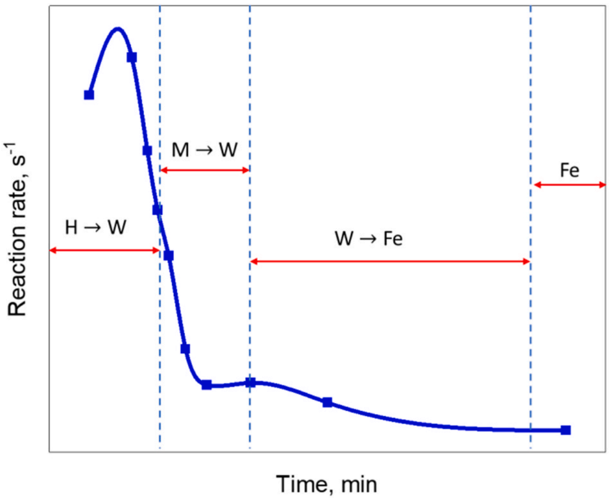

Fig. 5. Schematic of the reaction rate versus time for estimating the extent of H (H), M (M) to wustite (W), and wustite to Fe and Fe during the direct reduction of the pellets.

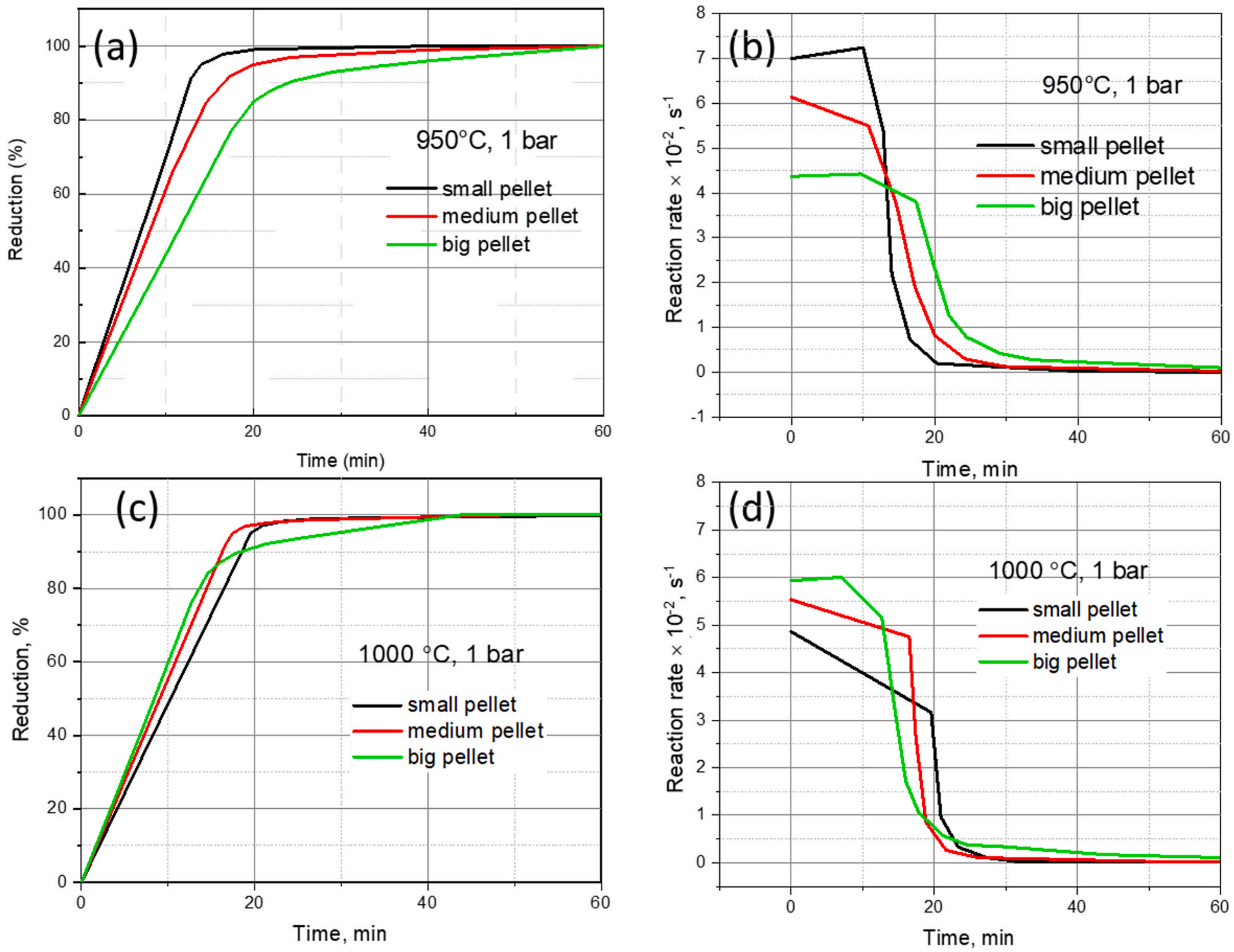

Fig. 6. (a,c)The reduction degree and (b,d)reaction rate as function of time at (a,b)950 °*C* and (c,d) 1000 °*C*.

Table 5
The estimated reduction rates for each reaction at 950 °*C* and 1000 °*C*. These rate values were extracted from Fig. 6.

Pellet	Reaction	Reduction rate × 10^{-2}, s^{-1}	
		950, °C	1000, °C
Small	H → M	7.2	4.26
	M → W	5.59	3.69
	W → Fe	0.79	2.91
Medium	H → M	7.1	5.21
	M → W	3.8	5.11
	W → Fe	0.65	3.31
Big	H → M	4.41	5.39
	M → W	2.65	5.04
	W → Fe	0.56	2.54

[a]H (H), M (M), wustite (W), and Fe.

min. Compared to the small pellets, both the small and the medium pellets have relatively smooth surfaces with minor irregularities in the unreduced state. In the reduced state, the small pellet developed a crack, while the medium pellet (Fig. 8 (b)) also showed surface changes, with the appearance of more pronounced deformations and roughness, although a clear crack was not as obvious as in the small pellet. In terms of porosity development, the porosity of the small pellet was evenly distributed in all directions in the unreduced state. After reduction, the porosity appeared to grow together, especially in the X and Y directions. The porosity of the medium pellet was also relatively uniform in the unreduced state. In the reduced state, the porosity was slightly larger and there were signs of coalescence, but not as pronounced as in the small pellet. The porosity in the reduced state of the medium pellet appeared to be more evenly distributed and the overall increase in pore size was less dramatic.

Fig. 9 shows microtomographic images of a large pellet before (unreduced state, images a-a3) and after (images b-b3), direct reduction at 950 °C for 90 min. In comparison with the previously provided images of the small and medium pellets, it can be seen that the external morphology of the small, medium and large pellets in the unreduced state has smooth surfaces with few features. The large pellet in Fig. 9 (a) appears to be similar to the medium and small pellets before reduction, with some surface roughness and irregularities. In the reduced state, the large pellet in Fig. 9 (b) has a cracked and deformed surface, similar to the medium pellet but more pronounced than the small pellet. In addition, the porosity distribution in the unreduced state was relatively evenly distributed across the X, Y and Z cross-sections for all pellet sizes. It should be noted that all pellets underwent changes in porosity after reduction. The small pellets showed a marked increase in pore size and connectivity, while the medium sized pellets showed increased porosity, with some signs of coalescence. The large pellet in Fig. 10 also showed an increase in porosity and coalescence in the cross-sections (b1, b2, b3), with the pores becoming more prominent and linear features forming that could indicate cracking. Therefore, cracking was observed in all pellet sizes after reduction.

Figs. 10–12 show microtomographic images of a small, medium and large pellet showing its morphology and internal structure before and

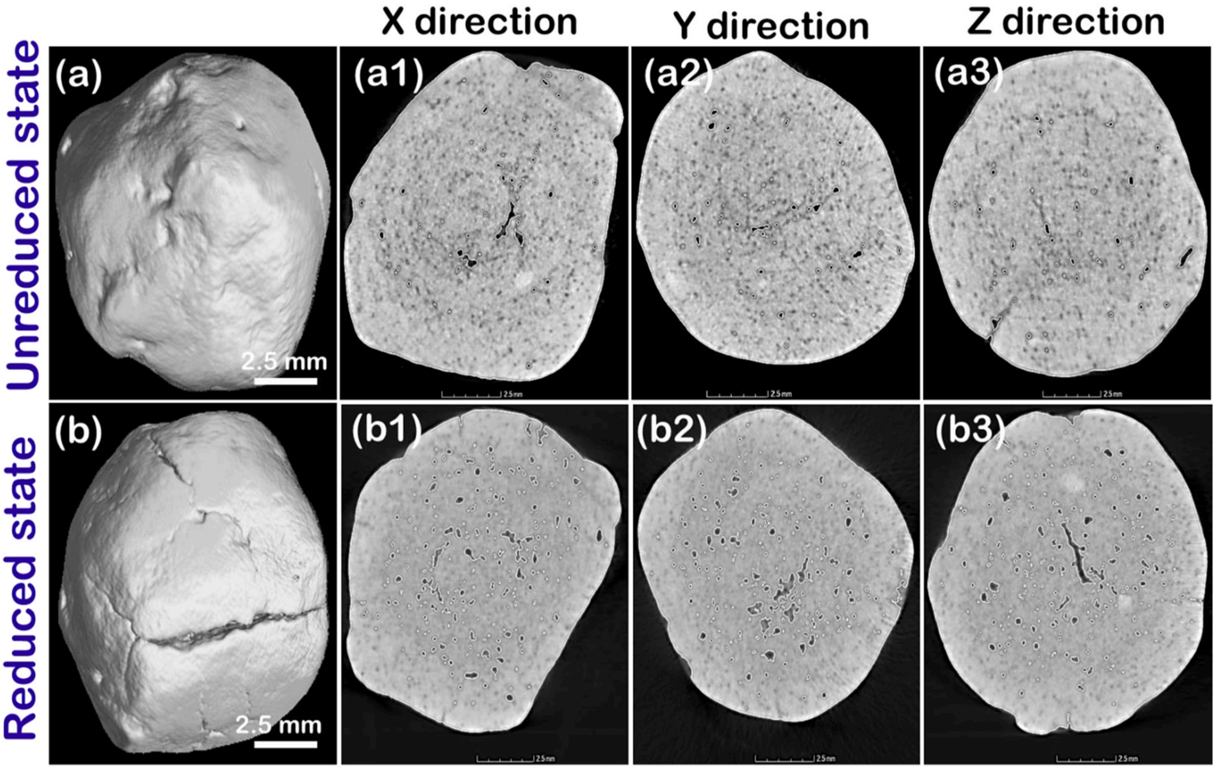

Fig. 7. Microtomographic appearance of small pellet before and after direct reduction at 950 °*C* for 90 min in (a-a3) unreduced state, and (b-b3) reduced state; (a1-a3 and b1-b3)cross-sectipellets the porosity evolution of the investigated°Cpellets mindirections (a1,b1) X, (a2,2)Y and (a3,b3) Z.

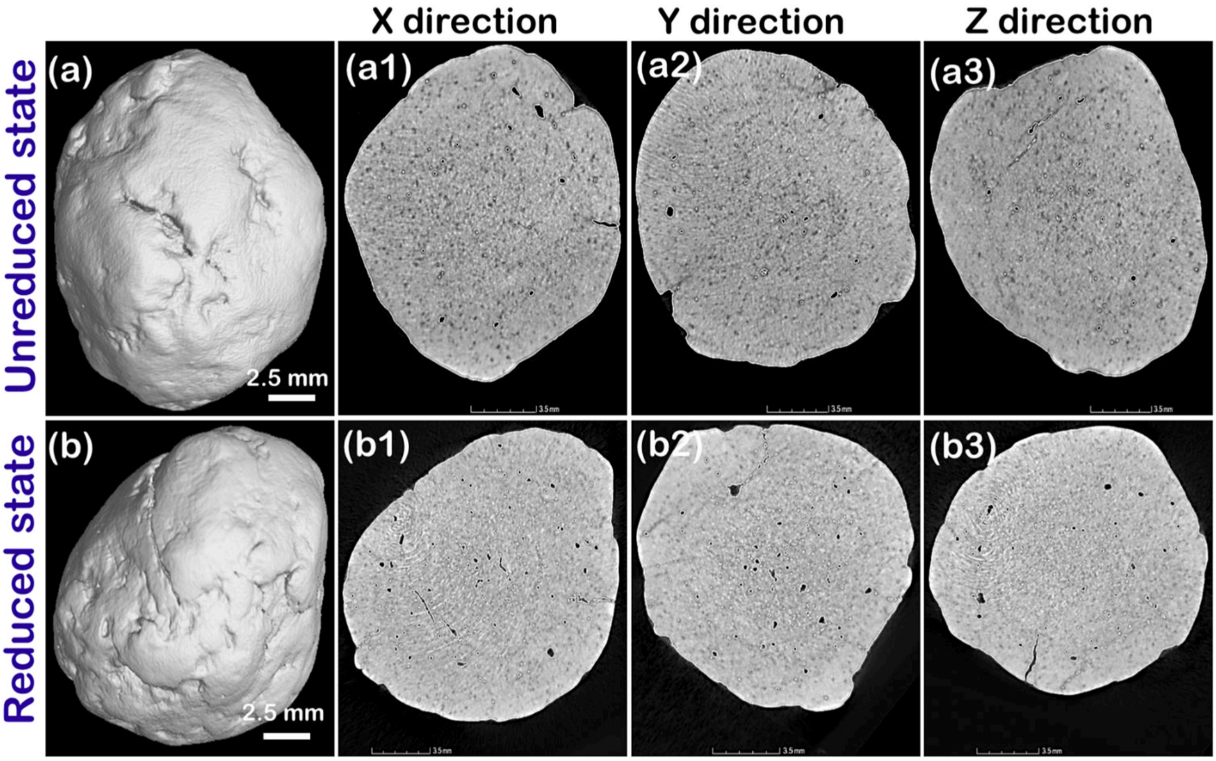

Fig. 8. Microtomographic appearance of medium pellet before and after direct reduction at 950 °*C* for 90 min in (a-a3) unreduced state, and (b-b3) reduced state; (a1-a3 and b1-b3)cross-sectipellets the porosity evolution of the investigated°Cpellets mindirections (a1,b1) X, (a2,b2)Y and (a3,b3) Z.

after direct reduction at 1000 °C for 90 min. After reduction, the pores in the small pellets show a tendency to merge and form interconnected networks, especially in Fig. 10 (b1) and (b2). The medium pellet showed a similar increase in porosity, with visible growth and coalescence of the pores. The porosity became more pronounced and interconnected, suggesting that higher temperatures favoured the coalescence of

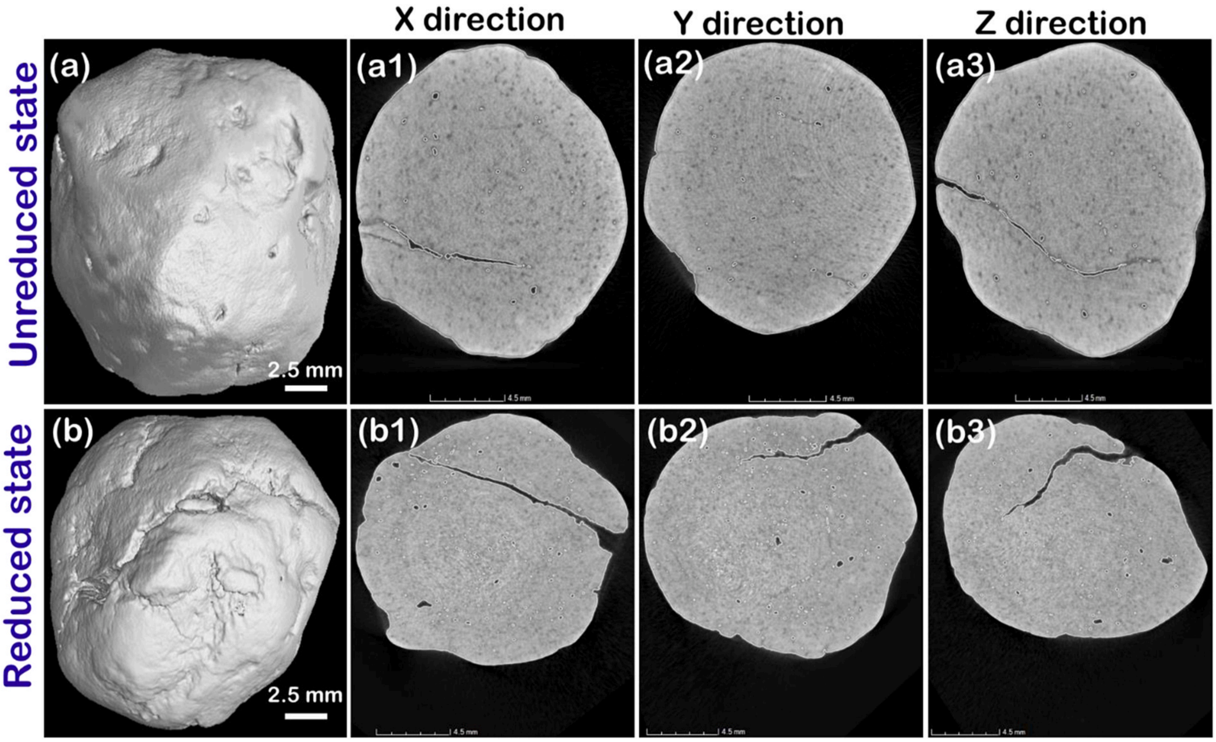

Fig. 9. Microtomographic appearance of big pellet before and after direct reduction at 950 °*C* for 90 min in (a-a3) unreduced state, and (b-b3) reduced state (a1-a3 and b1-b3)crosslargecpelletsof the porosity evolution of the investigat°Cd pelletmine directions (a1,b1) X, (a,b2)Y and (a3,b3) Z. (a2,b2,c2).

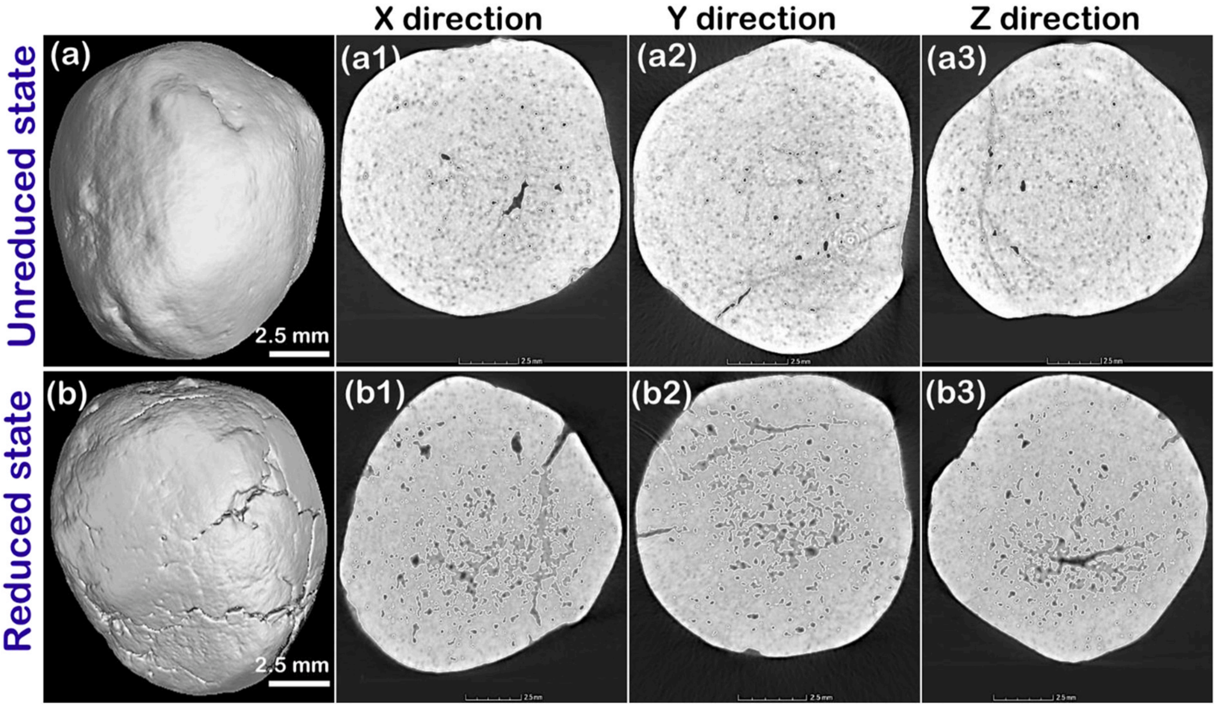

Fig. 10. Microtomographic appearance of small pellet before and after direct reduction at 1000 °C for 90 min in (a-a3) unreduced state, and (b-b3) reduced state; (a1-a3 and b1-b3)cross-sections of the porosity evolution of the investigated pellets in the directions (a1,b1) X, (a2,b2)Y and (a3,b3)Z.

individual pores into larger voids. For the large pellets, the increase in porosity after reduction was greatest for all three sizes. The pores in the large pellet not only increased in size, but also formed complex interconnected networks that spanned the cross-section of the pellet. This suggests that a larger pellet volume may have allowed a higher degree of porosity evolution. As for cracking, the surface of the small pellet appeared rougher with visible cracks after reduction. The cracks were present but appeared to be less extensive compared to the larger pellets, possibly due to the smaller size leading to less internal stress accumulation during reduction. The medium sized pellet exhibited significant surface deterioration with distinct cracks. The large pellet thus exhibited the most pronounced cracks both on the surface and in the internal

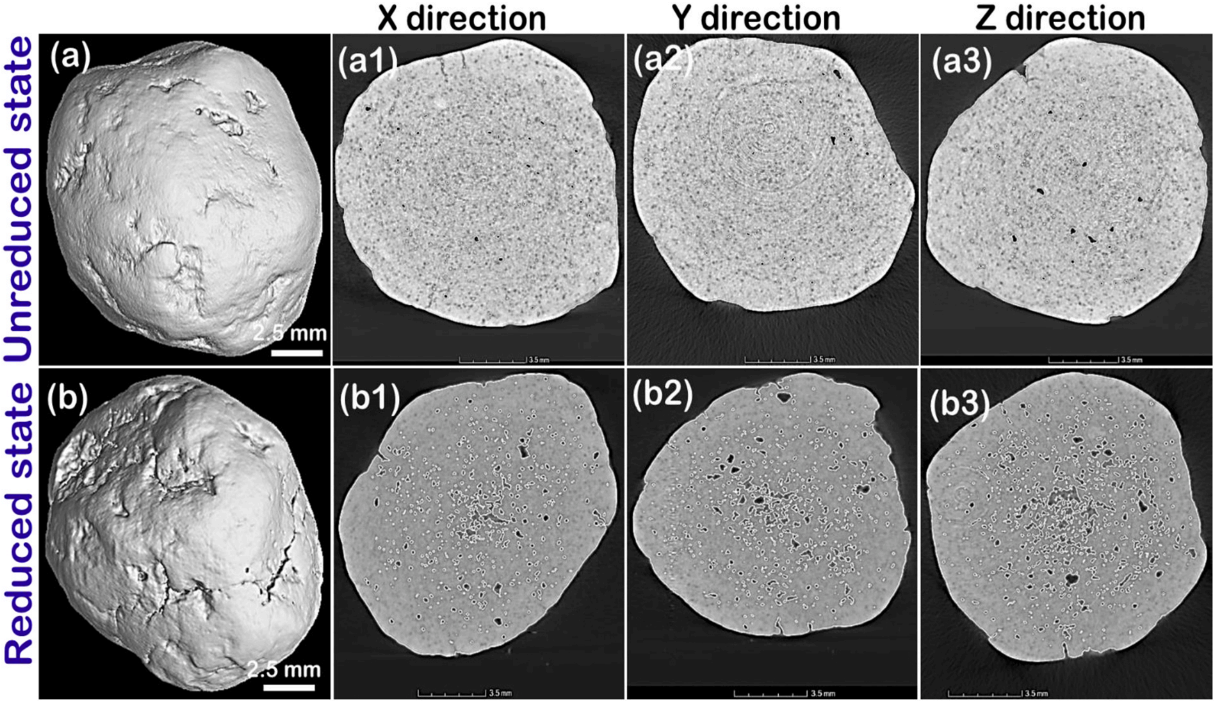

Fig. 11. Microtomographic appearance of medium pellet before and after direct reduction at 1000 °C for 90 min in (a-a3) unreduced state, and (b-b3) reduced state; (a1-a3 and b1-b3)cross-sections of the porosity evolution of the investigated pellets in the directions (a1,b1) X, (a2,b2)Y and (a3,b3)Z.

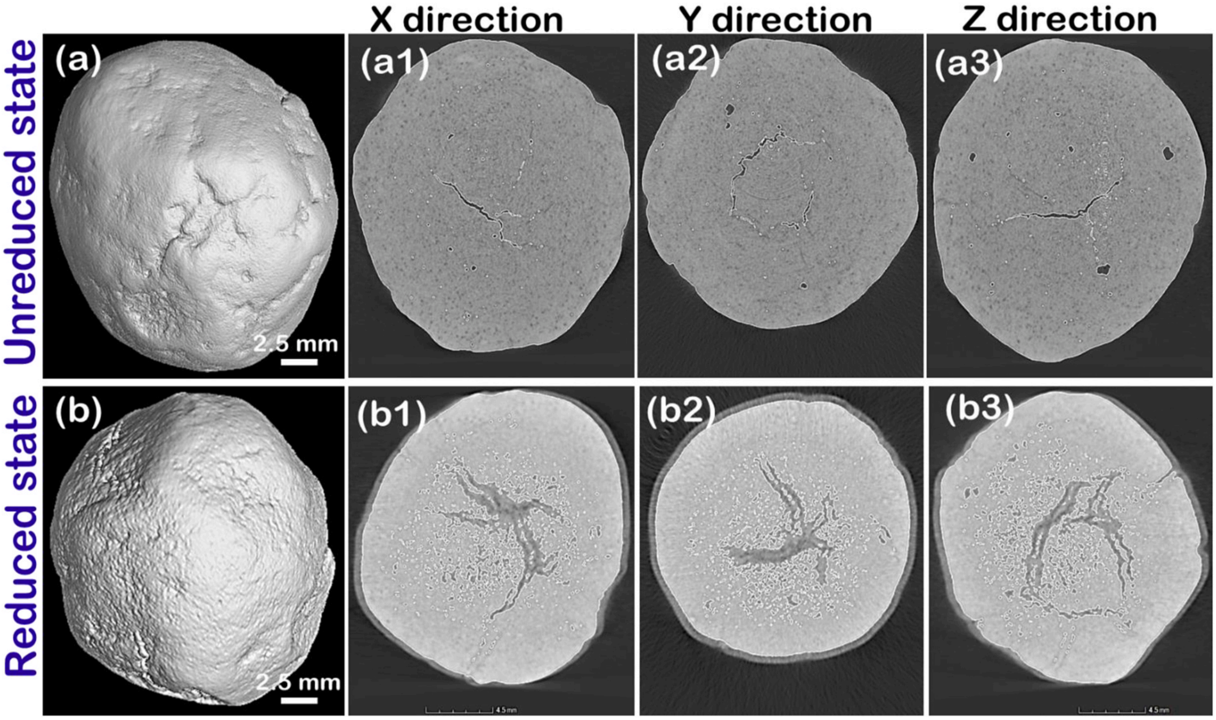

Fig. 12. Microtomographic appearance of big pellet before and after direct reduction at 1000 °C for 90 min in (a-a3) unreduced state, and (b-b3) reduced state; (a1-a3 and b1-b3)cross-sections of the porosity evolution of the investigated pellets in the directions (a1,b1) X, (a2,b2)Y and (a3,b3)Z.

structure.

Figs. 13 and 14 show the changes in pore properties and the evolution over time of a small pellet subjected to direct reduction at 950 °C and 1000 °C respectively. Fig. 13 (a) shows the pellet after 5 min. The pores are small and well distributed throughout the material. These pores are probably due to the original microstructure of the pellet before the reduction process started. Fig. 13(b) after 30 min shows a slight increase in pore size and some cases where the pores start to merge, indicating the onset of microstructural changes even in the unreduced state, possibly due to thermal effects. After 90 min, as can be seen in Fig. 13 (c), some pores have merged to form larger and more complex structures, indicating that even without reduction, prolonged exposure

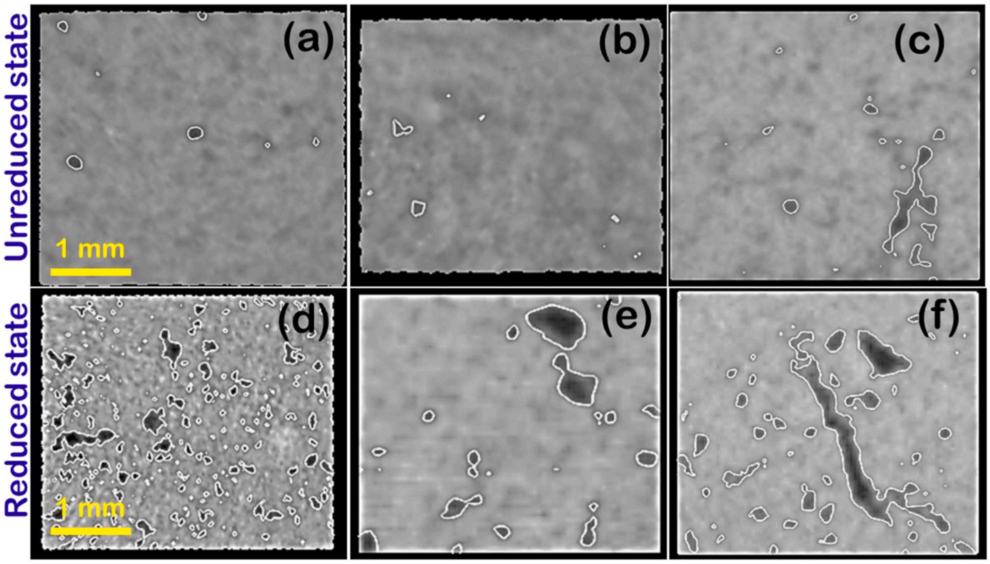

Fig. 13. Pores aspects and evolution as function of reduction time for the small pellet before and after direct reduction at 950 °C for (a,d)5 min, (b,e) 30 min, and (c, f) 90 min.

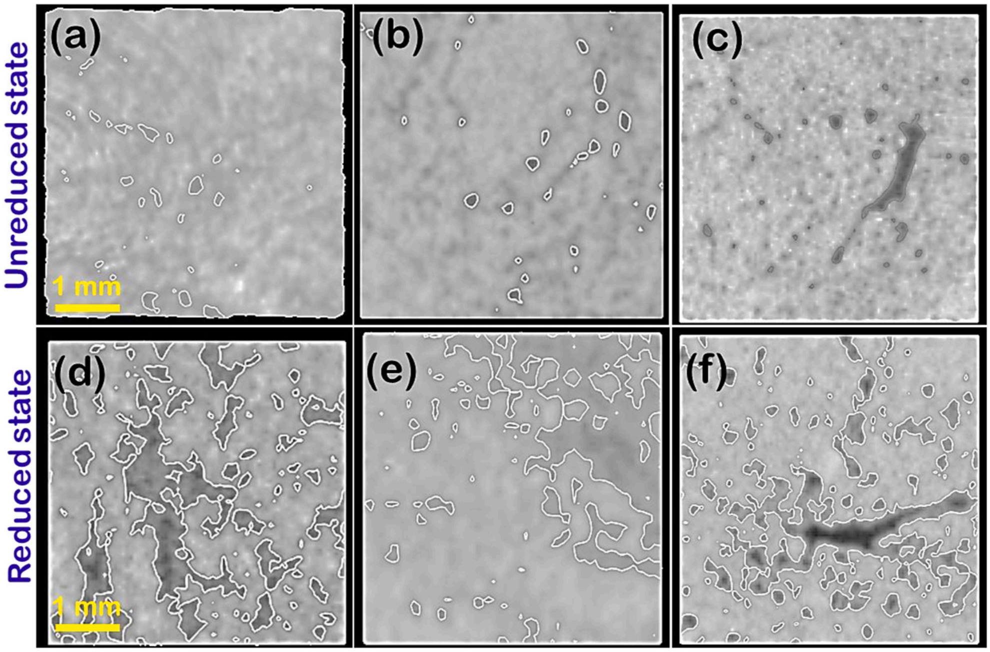

Fig. 14. Pores aspects and evolution as function of reduction time for the small pellet before and after direct reduction at 1000 °C for (a,d)5 min, (b,e) 30 min, and (c, f) 90 min.

to high temperatures can promote microstructural evolution. After 5 min of reduction, Fig. 13 (d) shows a clear contrast to the unreduced state. The pellet exhibits a high pore density, many of which are larger and more irregularly shaped, indicating a rapid change in porosity as a result of the reduction process. After 30 min, Fig. 13 (e) shows further growth and coalescence of the pores. The pore shapes are more diverse and the boundaries between the pores are less pronounced, reflecting the ongoing effects of reduction. After 60 min of reduction, Fig. 13 (f) shows extensive coalescence of the pores, resulting in large interconnected pore structures. This shows the peak of the microstructural changes caused by the reduction, with both the size and interconnectedness of the pores having changed significantly. Fig. 14(a) after 5 min shows sparse, small pores. After 30 min, as shown in Fig. 14(b), the pores appear slightly larger, indicating thermal effects, although no reduction has taken place. After 90 min (see Fig. 14(c)), the onset of pore growth and coalescence can be observed, a trend that continues over time even before reduction.

After 5 min of reduction, as shown in Fig. 14 (d), the pellet shows a clear increase in porosity with larger and better cross-linked pores. After 30 min (see Fig. 14 (e)), the pores have grown further and have formed a more interconnected network, a sign of progressive microstructural evolution due to the reduction. Finally, Fig. 14 (f) shows that after 90 min, the pellet exhibits extensive fusion of the pores, resulting in large interconnected channels, indicating significant structural changes. Fig. 15 shows the microtomographic appearance of the pores in small, medium and large pellets after direct reduction for 30 min at two different temperatures: 950 °C and 1000 °C. It is obvious that at 950 °C, as shown in Fig. 15 (a), the small pellet has small, well-defined pores

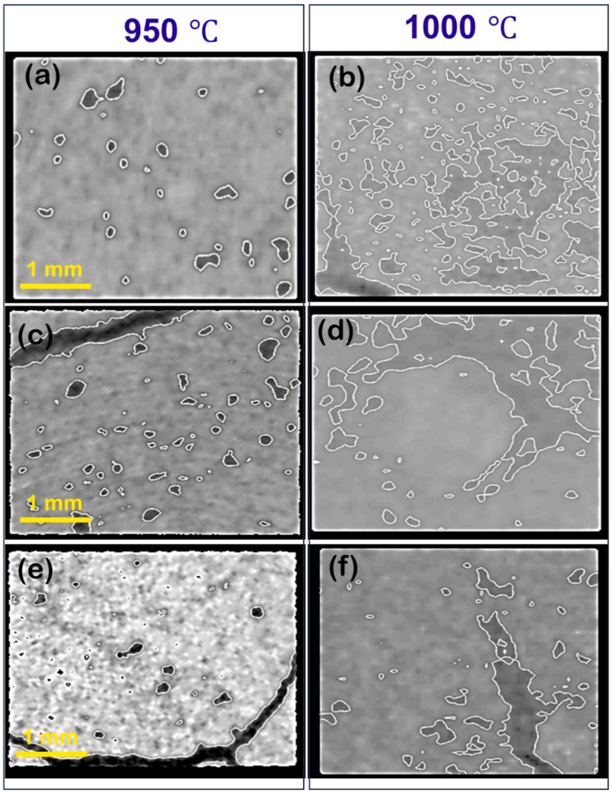

Fig. 15. Pores aspects and evolution as function of pellet size after direct reduction for 30 min, (a,b) small, (c,d) medium, (e,f)big.

with a slight coalescence. In contrast, at 1000 °C, as seen in Fig. 15 (b), the pores are much more numerous, larger and interconnected, indicating a more pronounced porosity evolution due to the higher temperature.

At 950 °C, the medium pellet shows larger pores compared to the small pellet at the same temperature, with some pores merging together (see Fig. 15 (c)). At 1000 °C, as seen in Fig. 15 (d), the porosity is significantly increased, with extensive coalescence and larger interconnected pore networks. At 950 °C (see Fig. 15 (e)), the large pellets have a slightly larger pore distribution than the small and medium pellets, with a relatively heterogeneous pore distribution. Even at 1000 °C, as shown in Fig. 15 (f), the porosity appears similar to the medium pellet, with large interconnected pores, although the overall porosity appears lower compared to the medium pellet at the same temperature. Tortuosity is an important factor in the discussion of porosity development in HyDR, as it can significantly affect the transport properties within the pellet, such as diffusivity and permeability. In this context, all microtomographs show greater porosity and cross-linking of the pores at 1000 °C compared to 950 °C. Although this indicates an increased permeability due to larger pores, the complexity of the pore network, namely the tortuosity, can also increase. A high tortuosity means that the path for the gas to diffuse through the pellet is more tortuous and complex, which could slow down the reduction process despite the increased porosity. In addition, the microtomographs show that the smaller pellets tend to have a faster development of porosity with a higher rate of interconnected pore formation, especially at 1000 °C. This may result in higher tortuosity as the smaller volume of the pellet may restrict the growth and direction of the pore channels, resulting in a more tortuous path. Larger pellets could have a more uniform pore distribution with potentially lower tortuosity. The peak in porosity rate indicates a point where porosity increases most rapidly, which could be associated with a period where tortuosity also develops rapidly. After the peak, the reduction in porosity rate could be influenced by the increase in tortuosity, which hinders the further development of porosity as it is difficult to remove additional material without extensive new pore formation.

Fig. 16 shows the calculated change in porosity as a function of time during HyDR at two different temperatures. Across all pellet sizes, an increase in porosity with time can be observed at both temperatures. It is notable that porosity increases rapidly at 1000 °C for each pellet size before reaching a peak and then decreasing. This trend is particularly pronounced and occurs earlier compared to 950 °C. At 950 °C, as shown in Fig. 16(a), the porosity of the small pellets increases steadily over time, surpassing the porosity values of the medium and large pellets. This behaviour highlights the fact that smaller pellets, with their larger surface area relative to volume, are likely to undergo more efficient gas-solid interactions, allowing for a faster increase in porosity. Conversely, the medium and large pellets show a more gradual increase in porosity, with the large pellets showing the most significant overall increase at the end of the reduction time. Looking at the results at 1000 °C (see Fig. 16 (b)), there is a sharp increase in porosity for all pellet sizes, reaching a maximum faster than at the lower temperature. This peak value, followed by a decrease in porosity, indicates an increased reaction rate at the higher temperature. The earlier onset of porosity stabilisation or reduction at 1000 °C could be due to accelerated reduction kinetics driving the transition to the sintering phases, or to material consumption subsequently preventing further porosity development.

Fig. 17 provides contour maps at three time points (10, 30, and 90 min) that illustrate the porosity distribution within each pellet, with warmer colors indicating higher porosity and cooler colors indicating lower porosity. For the small pellets in Fig. 17(a), at both temperatures, the porosity is initially concentrated in certain regions and becomes more uniform over time. At 1000 °C, the porosity increases more rapidly and to a greater extent than at 950 °C, covering a larger area of the pellet. For medium pellets given in Fig. 17 (b), a similar pattern is seen with porosity developing and spreading over time. Again, the porosity at 1000 °C is more extensive than at 950 °C, particularly at the 30 and 90-min marks. Lastly, the big pellets in Fig. 17(c) demonstrates the porosity changes are less pronounced at 950 °C, with some regions showing minimal porosity even after 90 min. At 1000 °C, the increase in porosity is more noticeable, but the distribution is uneven, with some areas experiencing significant porosity while others remain relatively unchanged.

When the temperature is increased to 1000 °C, the microstructure in both the small and big pellets shows a significant increase in porosity, as can be seen in Fig. 18 (c) and (d). The small pellet at 1000 °C (c) exhibits larger voids compared to its counterpart at 950 °C (a), suggesting that temperature plays a significant role in the development of porosity, which is confirmed by the increased overall rates of porosity development at 1000 °C in Table 6. The bigger pellet at 1000 °C (Fig. 18 (d)) shows even more extensive pore formation, which is consistent with the trend of increased porosity at larger pellet size and higher temperatures.

The presence of iron is widespread and intense throughout the mapping, indicating a significant degree of reduction (Figs. 19 and 20). The silicon map shown in Fig. 20 highlights concentrated areas of silicon that are more pronounced than in the mapping of the small pellet from Fig. 19. This is attributed to the larger pellet size affecting the aggregation of silicon compounds, possibly due to slower reduction kinetics in the core of the pellet compared to its surface. In particular, Fig. 20 shows that calcium is present throughout the pellet, suggesting the presence of calcium in the gangue material. This uniform presence of calcium could also influence the reduction behavior and final microstructure of the pellet. Aluminum is sparsely distributed, similar to the findings in the small pellet, but is less concentrated in the large pellet. This could be due to the size of the pellet and the resulting influence on the distribution of non-ferrous elements during pellet formation and reduction. The oxygen map shows a significant number of white dots, indicating that oxygen is still present in the pellet. The distribution is not entirely uniform, which, when correlated with the porosity observed in the SEM image, suggests

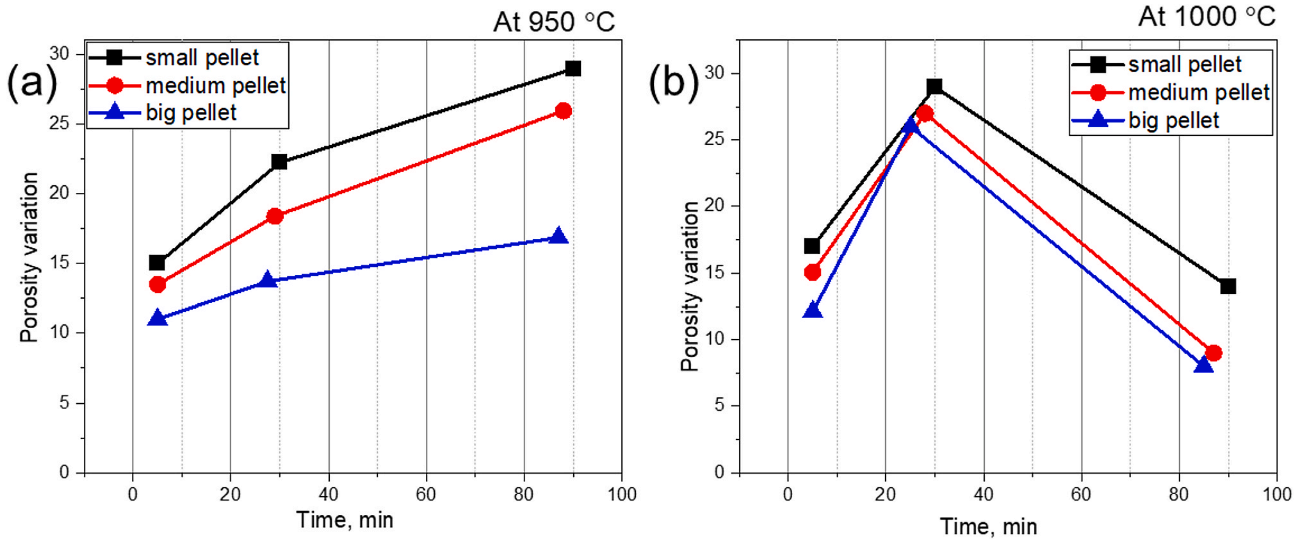

Fig. 16. The calculated porosity variation evolution over reduction time during HyDR at (a) 950 °C (b) 1000 °C.

that oxygen may be more abundant in areas of less void formation.

5. Discussion

In the direct reduction of iron oxide with hydrogen, the first two stages, i.e. the reduction of H to M and the reduction of M to W, are mainly controlled by the chemical reactions at the interfaces. In the third stage of reduction, i.e. the reduction of W to Fe, processes based on atomic diffusion are leading and suppress the reduction process [55,57]. For this reason, the morphology and physical properties of the pellets play an important role in creating the diffusion pathways at this stage. In this regard, the mass change during each process can have a significant impact on the formation and development of the type of pores, which in turn can influence the regeneration rate in each step of the reaction by providing an effective surface area that influences chemical reactions. Considering that porosity leads to a larger active surface area available for the chemical reactions in the first two stages of the reduction process, the development of porosity can lead to a larger contact area between hydrogen and iron oxides, which in turn leads to an increase in the reduction reaction rate in the first two stages of the process. However, in the third stage, atomic diffusion, which depends on the penetration of the material mass, can be influenced to a certain extent by porosity, so that the development of porosity can increase atomic penetration to a certain extent.

When comparing the results for different pellet sizes at 950 °C and 1000 °C, it can be seen that the higher temperature significantly increases the effects on porosity evolution and cracking for all pellet sizes, as shown in Fig. 21 (a) and (b).

In the simulated results shown in Fig. 21, small pellets show a more pronounced increase in porosity variation at both 950 °C and 1000 °C compared to medium and large pellets. Also, it is obvious that in all three pellet sizes, the porosity variation increases more rapidly at the higher temperature of 1000 °C compared to 950 °C (Fig. 22). This observed behaviour is consistent with the theoretical prediction and microtomographies images, which support the notion that smaller pellets, with their larger surface area relative to volume, allow for more effective gas-solid interactions and thus promote a faster reduction process. In addition, the simulation results show that for all pellet sizes, porosity variations are greater at 1000 °C than at 950 °C. This trend is consistent with the higher reaction rates at higher temperatures, as can be seen in Fig. 6 and Table 5. At 950 °C, the porosity variation increases gradually for small and medium pellets until it reaches a plateau at around 70 and 72 min respectively. In contrast, large pellets show a stronger increase in porosity variation and do not reach a plateau within the observed time period. At 1000 °C, the porosity variation increases rapidly for all pellet sizes and peaks at around 63, 64 and 66 min for small, medium and large pellets respectively. After these peaks, the porosity variation decreases slightly, possibly due to sintering or similar processes that reduce porosity at higher temperatures. In addition, the increase in temperature and porosity likely leads to increased diffusion coefficients, which explains the larger porosity variations observed at 1000 °C. The trends observed in the simulations reflect the known effects of pellet size and temperature on the HyDR process. Due to their larger surface area relative to volume, smaller pellets respond faster and reach higher porosity variations earlier than their larger counterparts. The modest decrease in porosity variation after peaking at 1000 °C indicates the presence of a compensating mechanism, possibly sintering, which becomes more important at higher temperatures and longer reaction times. The simulation results emphasize the importance of pellet size and temperature in the HyDR process. They confirm that smaller pellets exhibit larger porosity variations and higher temperatures contribute to increased porosity, although they can also lead to complex effects such as sintering in the later stages of reduction.

In addition, the calculated developments of the porosity variations agree with the contour maps. The smaller pellets reach higher porosity levels faster, indicating their faster response to the HyDR process. This can be explained by the fact that smaller pellets, with their larger surface area relative to volume, are more reactive, allowing the reducing gas to penetrate and react more thoroughly, resulting in higher porosity. With larger pellets, on the other hand, the lower surface area to volume ratio leads to slower reaction kinetics, so that the porosity develops more slowly and less uniformly, as can be seen in the contour maps for the big pellets at both temperatures. The pronounced increase in porosity and the increased cracking observed at 1000 °C are scientifically associated with the accelerated kinetics of diffusion and reaction processes due to the higher temperature, which intensifies pore growth and coalescence as well as cracking caused by thermal stresses. This is particularly noticeable in larger pellets at 950 °C, where the tendency for larger pores may be a result of their larger volume and the resulting internal stresses and structural changes. However, at 1000 °C, the differences in porosity between pellet sizes are less pronounced, suggesting that the influence of increased temperature on the reduction process outweighs the effects of pellet size, with increased reaction rates and atomic mobility contributing to a more uniform porosity development between the different sizes. From the microtomographs at 950 °C compared to 1000 °C, it can be interpreted that higher temperatures lead to greater

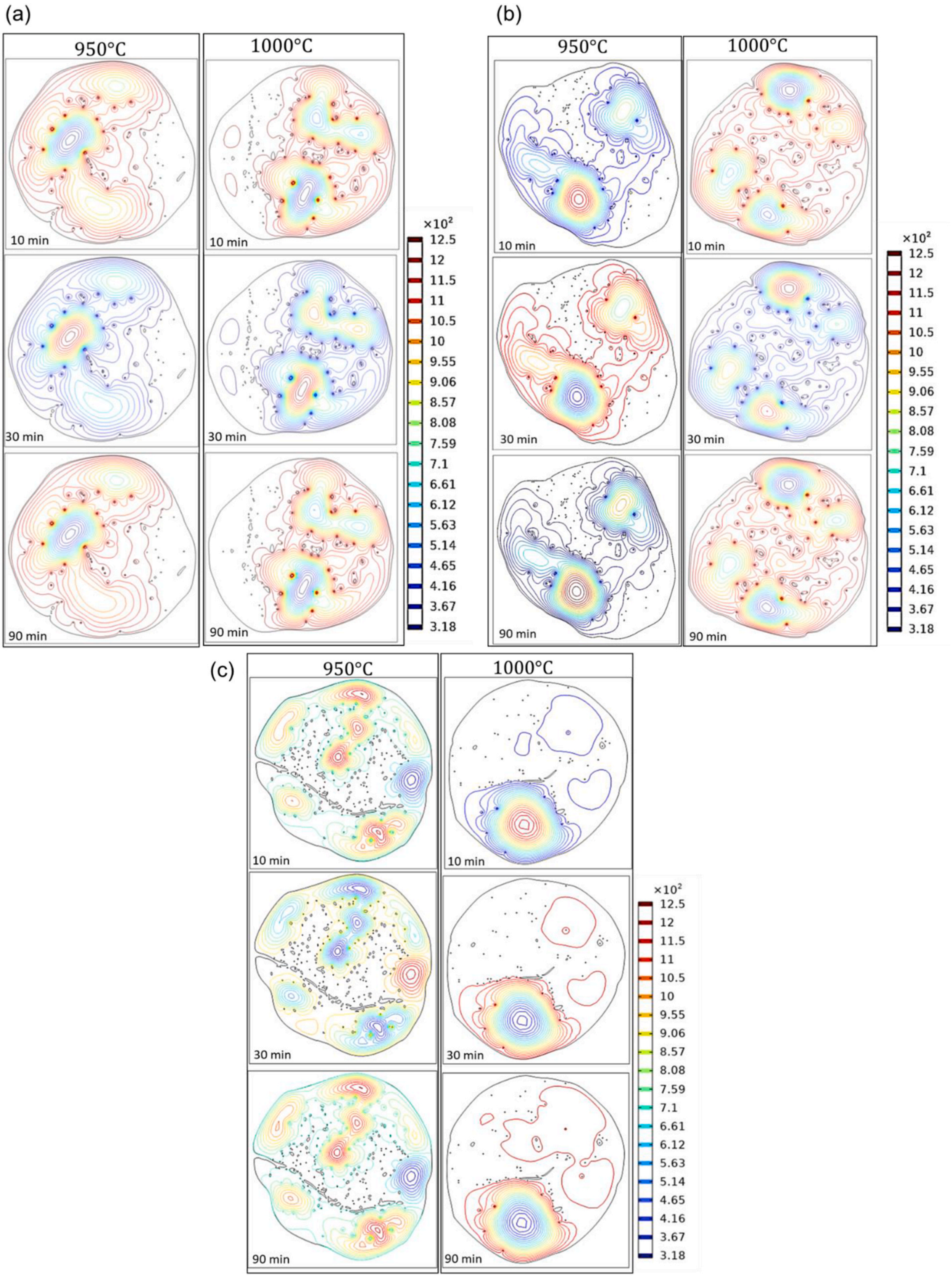

Fig. 17. The simulated results for the time-dependent change in porosity during HyDR at 950 °C and 1000 °C for 90 min for different pellet sizes (a) small, (b) medium and (c) big.

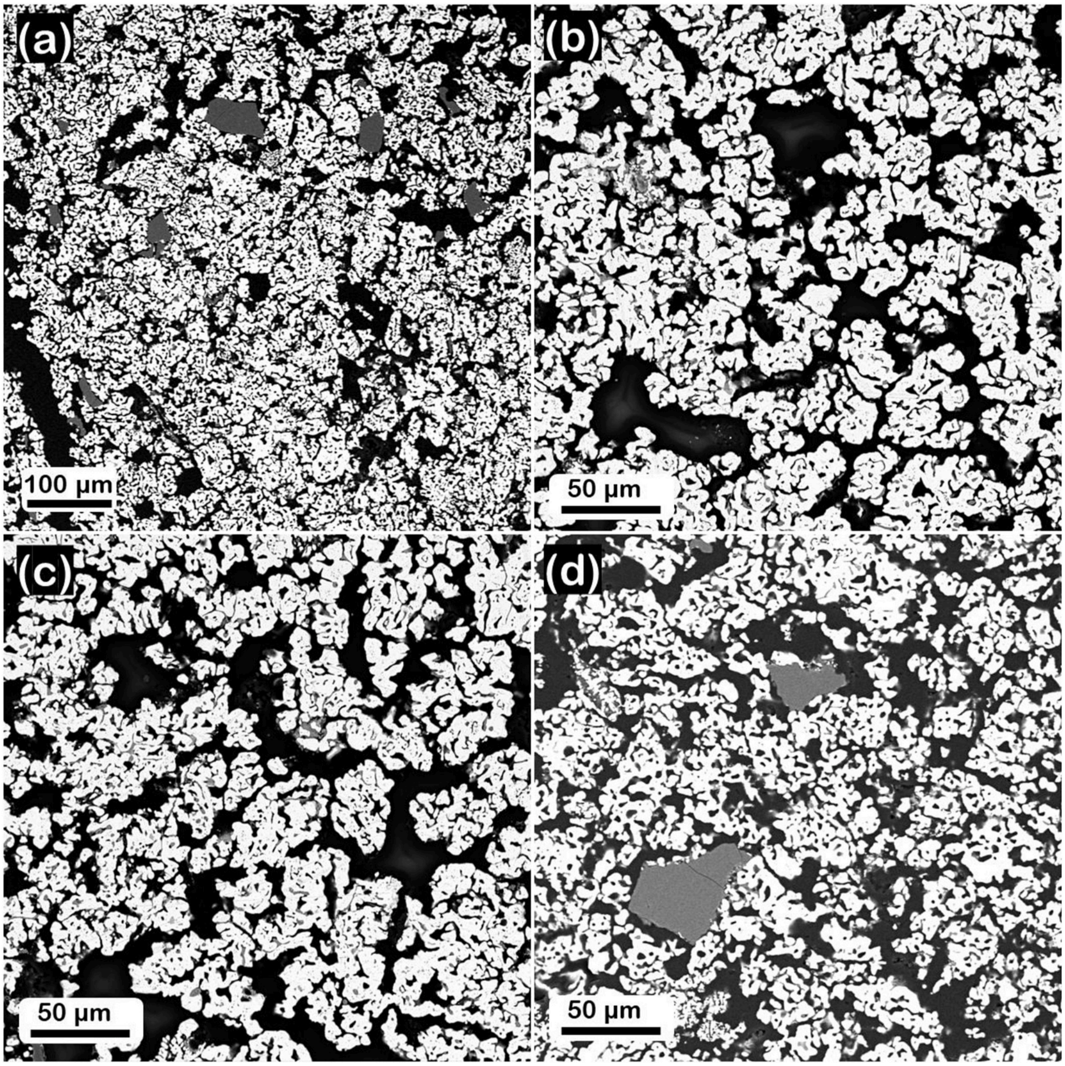

Fig. 18. SEM images showing the microstructure of reduced pellets at two different temperatures: (a, b) 950 °C and (b) 1000 °C for 90 min. In (a, c) a small pellet is shown, while (c, d) shows a larger pellet.

Table 6
Calculated porosity rate for intermediate and total reduction reactions for different pellet size at 950 °*C* and 1000 °*C*.

Temp. °C	Pellet	Porosity evolution rate			Total porosity evolution rate
		H → M	M → W	W → Fe	
950	small	3.13	4.76	0.28	**8.17**
	medium	5.74	4.14	0.22	**10.1**
	big	7.03	9.22	0.60	**16.85**
1000	small	4.50	4.81	1.00	**10.31**
	medium	4.13	5.26	1.20	**10.59**
	big	8.56	13.72	2.61	**24.89**

porosity and cracking. In addition, the rate at which porosity develops can be visually correlated with the extent and size of the pores in the microtomography images. For example, the microtomography images at 1000 °C showed a rapid development of large interconnected pores, which is consistent with the higher porosity rates at this temperature. In addition, the size of the pellets influenced the rate of porosity development, with smaller pellets showing a more pronounced rate of porosity increase at 1000 °C than medium and large pellets. This is consistent with the microtomographic images, where smaller pellets showed rapid changes, especially at higher temperatures. Furthermore, the time to reach the maximum porosity rate corresponds to the images where the strongest pore coalescence was observed. For example, at around 30 min, the microtomographs showed remarkable pore growth and connectivity, which is consistent with the peak values in Fig. 16. Comparison of the calculated porosity rate for the intermediate stages given in Table 6 shows that the rate of porosity development near the pellet surface is relatively high, so the tortuosity of the pores near the pellet surface is usually quite high. This results in a lower effective diffusion coefficient, which leads to a slow reduction rate, especially from W to Fe, in the late stages of HyDR. To justify these observations, an understanding of the kinetic behaviour of the reduction reactions during the HyDR process is required. The increased porosity rates at 1000 °C compared to 950 °C are due to the greater kinetic energy promoting the diffusion and reduction reactions. The temperature dependence of reduction kinetics means that higher temperatures accelerate reaction rates, leading to faster and more extensive microstructural changes, including the formation and expansion of pores. In addition, the observed decrease in porosity rate over time is explained by the depletion of the reducible material and the increasing difficulty of gas diffusion as larger pores develop, as well as possible sintering or restructuring of the pellet at higher temperatures, which can prevent further increases in porosity. The greater temperature gradient at 1000 °C could also cause a thermal shock that further intensifies crack development,

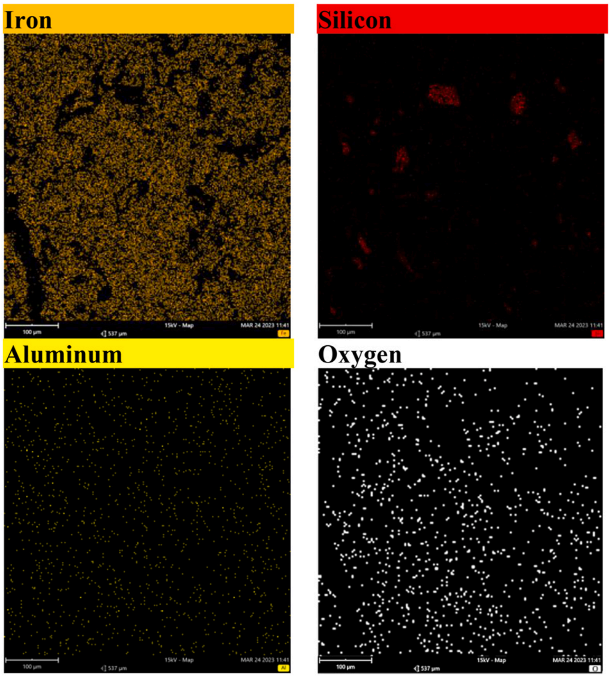

Fig. 19. Composition mapping of the small pellet reduced for 90 min at 950 °C (Fig. 18 (a) shows a corresponding SEM image).

suggesting that higher temperatures generally accelerate microstructural changes in materials that are thermally treated.

During HyDR, the reduction rate varies with time, assuming that the diffusion of H_2 to or H_2O from the pellet/gas interface is the rate-limiting step of the reaction [1]. This can be attributed to a continuously increasing specific surface area of the pellet and the corresponding change in gas permeability. However, the reduction rate of the intermediate reactions over the entire HyDR shows a relatively stable reduction rate for all pellet sizes within the reduction degree range of ~0.56–~7.2 for 950 °C and ~2.54 to ~5.39 for 1000 °C. It is important to note that at lower reduction temperatures, 950 C in this case, the reduction rate ranges from ~0.33 to ~0.7, especially for small pellet sizes, as reported in Ref. [1]. For most of the reduction rates calculated in the present work, the reduction rates are an order of magnitude higher than those reported in the literature [1,19]. This can be attributed to several reasons, such as a higher reduction temperature and a higher porosity content in both the unreduced and reduced states. In particular, the high porosity and tortuosity, i.e. the degree of percolation topology of the inner free surface areas, provide fast diffusion pathways for the reactants and abundant potential nucleation sites. The accessibility of the inner surfaces to the reducing gas significantly accelerates the global reduction kinetics. It also plays an essential role in the uptake and removal of the oxidation product, i.e. the water produced during the redox reaction.

Table 6 shows that the porosity evolution rate is positively correlated with the pellet size across both temperatures and reduction stages. In particular, small pellets at 950 °C show the lowest porosity evolution rate during the transition from H to M, while big pellets show the highest rates. This trend also applies to the subsequent stages of reduction, with big pellets showing the most significant increase in the overall porosity evolution rate. At the elevated temperature of 1000 °C, it again can be seen a reinforcement of this pattern, with porosity rates for equivalent sizes exceeding those at 950 °C, suggesting that higher temperatures promote porosity evolution. In particular, during the final reduction step from W to Fe, the porosity evolution rate increases dramatically, especially for big pellets.

As seen from Table 6, the small pellets show a higher porosity evolution rate (4.76) during the M to W phase than the medium (4.14) and big pellets (9.22). This could be due to the smaller pellets having more surface curvature, which could increase surface reactivity and allow for faster reduction kinetics, although the overall trend is less clear and could be influenced by other factors such as gas diffusion dynamics. The curvature effect can be an important factor in the HyDR of iron oxide pellets and influence the reduction kinetics and porosity evolution [58]. In the final stages of W-to-Fe reduction at 950 °C, porosity rates are significantly lower in all sizes, suggesting that the curvature effect is less effective in the final stages of reduction, possibly due to the slowing of reaction kinetics as the reduction nears completion. At 1000 °C, porosity evolution rates generally increase for all pellet sizes, suggesting that higher temperatures mitigate the curvature effect by improving reduction kinetics throughout the pellet and not just at the surface. For big pellets, the porosity evolution rate jumps significantly from H to M to 8.56, indicating that temperature can enhance the curvature effect for larger pellets, possibly due to better heat transfer and reaction rate. The M to W stage at 1000 °C shows increased porosity evolution rates for all sizes, with the largest effects observed for medium (5.26) and large (13.72) pellets. The curvature effect is pronounced in larger pellets, where the lower surface area to volume ratio can lead to a greater accumulation of hydrogen on the pellet surface, which increases the reduction rate and porosity evolution. Smaller pellets, which have a greater curvature, tend to distribute stresses more evenly during

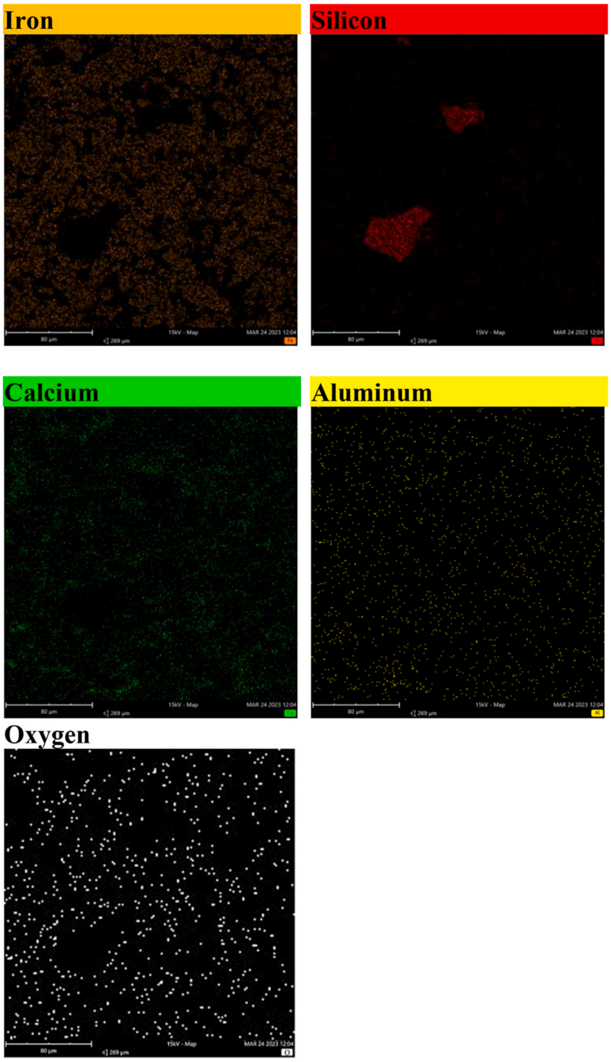

Fig. 20. Composition mapping of the big pellet reduced for 90 min at 950 °C (Fig. 18 (d) shows a corresponding SEM image).

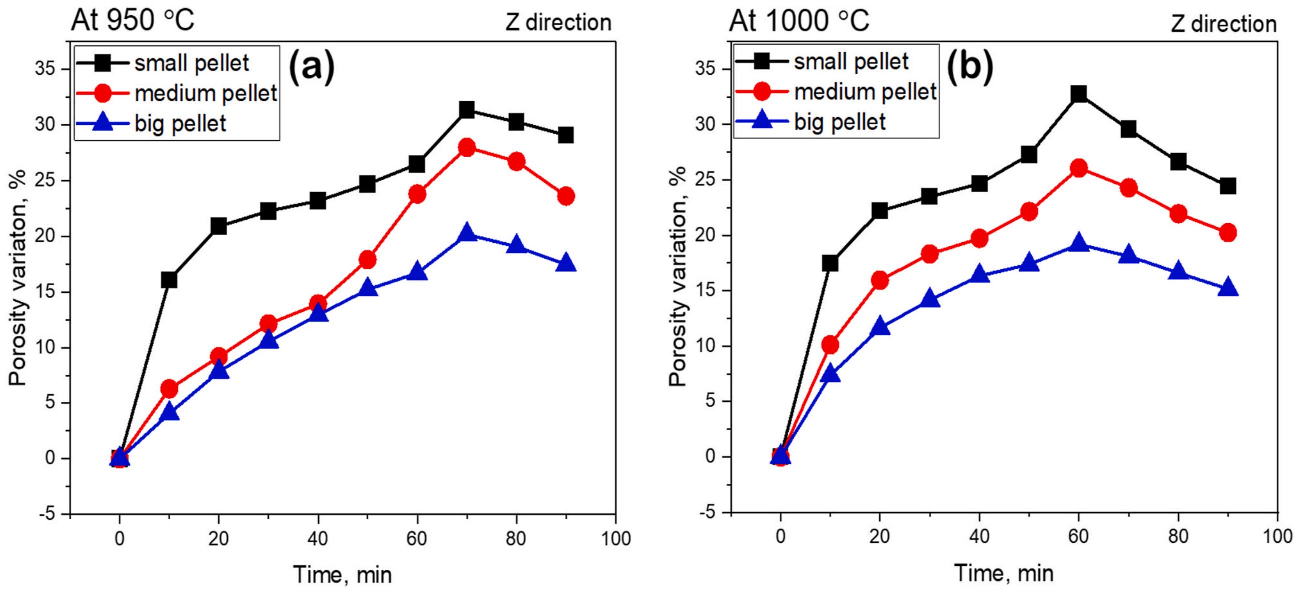

Fig. 21. The porosity variation (comes from simulated results) over reduction time during HyDR for different pellet size (a) 950 °C (b) 1000 °C.

reduction, resulting in lower porosity. In contrast, larger pellets with less curvature are more prone to uneven stress distribution, which can lead to increased porosity and a higher probability of cracking. This effect, combined with the inherent differences in geometry and curvature of pellets of different sizes, contributes to the observed differences in density and porosity distribution, with larger pellets being more prone to the formation of internal voids and less dense regions. Therefore, it can be concluded that the curvature effect together with the improved thermal conditions may favor a more uniform reduction in pellet volume. In addition, the overall rates of porosity development also reflect the combined effects of temperature and curvature, with the greatest overall change observed for big pellets at 1000 °C (24.89). This could be due to the larger pellets being better able to maintain a higher porosity throughout the reduction process when exposed to higher temperatures, despite their lower surface area to volume ratio.

From a kinetic point of view, the higher rate indicates that the entropy generated by chemical reactions is greater at 1000 °C because the reactions take place faster [10]. In addition, higher temperatures and larger pellets can be shown to have higher rates, indicating an increase in porosity. This increase in porosity can lead to a decrease in entropy generation as gas penetration is improved and flow resistance s reduced [1,55]. The higher porosity evolution rates at higher temperatures and in larger pellets cause an increase in pore complexity and tortuosity (see Table 1S). The interplay between pore structure and gas flow dynamics, especially diffusion and convection in porous media, plays a crucial role in the HyDR process of iron oxide pellets [59]. Table 6 shows that the porosity evolution rate varies significantly with pellet size and temperature, which in turn influences the gas transport mechanisms. Figs. 22 and 21 also illustrate that with increasing porosity, especially at higher temperatures, there is a greater free volume for gas flow, which promotes both diffusion and convection within the pellets. The observed trend shows that larger pellets and higher temperatures lead to greater porosity variation, which can result in more pronounced convective behavior. This is likely due to the larger pathways available for gas movement and the thermal expansion of gasses at higher temperatures. Consequently, this affects the reduction kinetics, with larger pellets exhibiting a faster increase in porosity at 1000 °C and a steeper decline after the peak, suggesting changes in the dominant gas flow mechanism as the reduction progresses. In addition, the curvature of the pellets has a significant effect on the surface area available for gas-solid interactions. Smaller pellets with higher curvature have a greater surface area to volume ratio, which improves contact between the reducing gas and the iron oxide surface. This larger contact area allows for more uniform and efficient reduction throughout the pellet. Conversely, larger pellets with less curvature have a smaller surface area in relation to their volume, which can lead to less uniform reduction. The reason for this is a more pronounced concentration gradient of the reducing gas in the pellet, which can lead to uneven reduction and localized zones with higher porosity. In addition, the shape of the pellet influences the path and flow rate of the gasses in the void spaces, which affects the overall reduction kinetics.

The increased tortuosity can act as an obstacle to gas flow, and reduce diffusion and the reduction effect, prolonging the time to reduction [10]. The high porosity rates for large pellets at 1000 °C imply that the tortuosity is also likely to be higher, which can lead to increased entropy generation. Entropy generation increases with the decrease in porosity and gas fraction due to the reduced exchange surfaces [1,2]. This is because the lower porosity rates for small pellets at 950 °C compared to larger pellets at 1000 °C, where the reduced exchange surfaces could lead to increased entropy generation. This more likely has a significant effect on the W → Fe transition as a sluggish step. The data given in Table 5 show that the reduction rate for the W → Fe transition increases significantly for all pellet sizes at 1000 °C compared to 950 °C. This increase in rate could reduce the entropy generation by chemical reactions as the reactions occur faster, despite the increased tortuosity. It can be concluded that at higher temperatures, the increased reduction rates and porosity evolution rates lead to higher entropy generation due to chemical reactions but possibly lower entropy generation due to mass transfer as gas penetration improves. However, the increased tortuosity at higher temperatures and in larger pellets may increase entropy generation due to the additional resistance to gas flow. The total energy input to the reduction process is a balance between these factors and would be higher for processes that generate more entropy, especially in the initial stages of reduction where both the chemical reaction and gas diffusion are rate-limiting steps. As the process progresses, the thermal gradient and the driving force for the chemical reactions reduce, leading to a decrease in entropy generation.

The reduction process carried out at 950 °C for 90 min leads to an increase in free volume of approx. 3.5%, while at 1000 °C the free volume increases by a smaller margin of 0.26%. At the same time, a decrease in the average pore diameter can be observed at both temperatures. This indicates that the microstructural transformation of the pellets during reduction is not only a product of their initial porosity, but is also characterized by an increase in free volume and the introduction

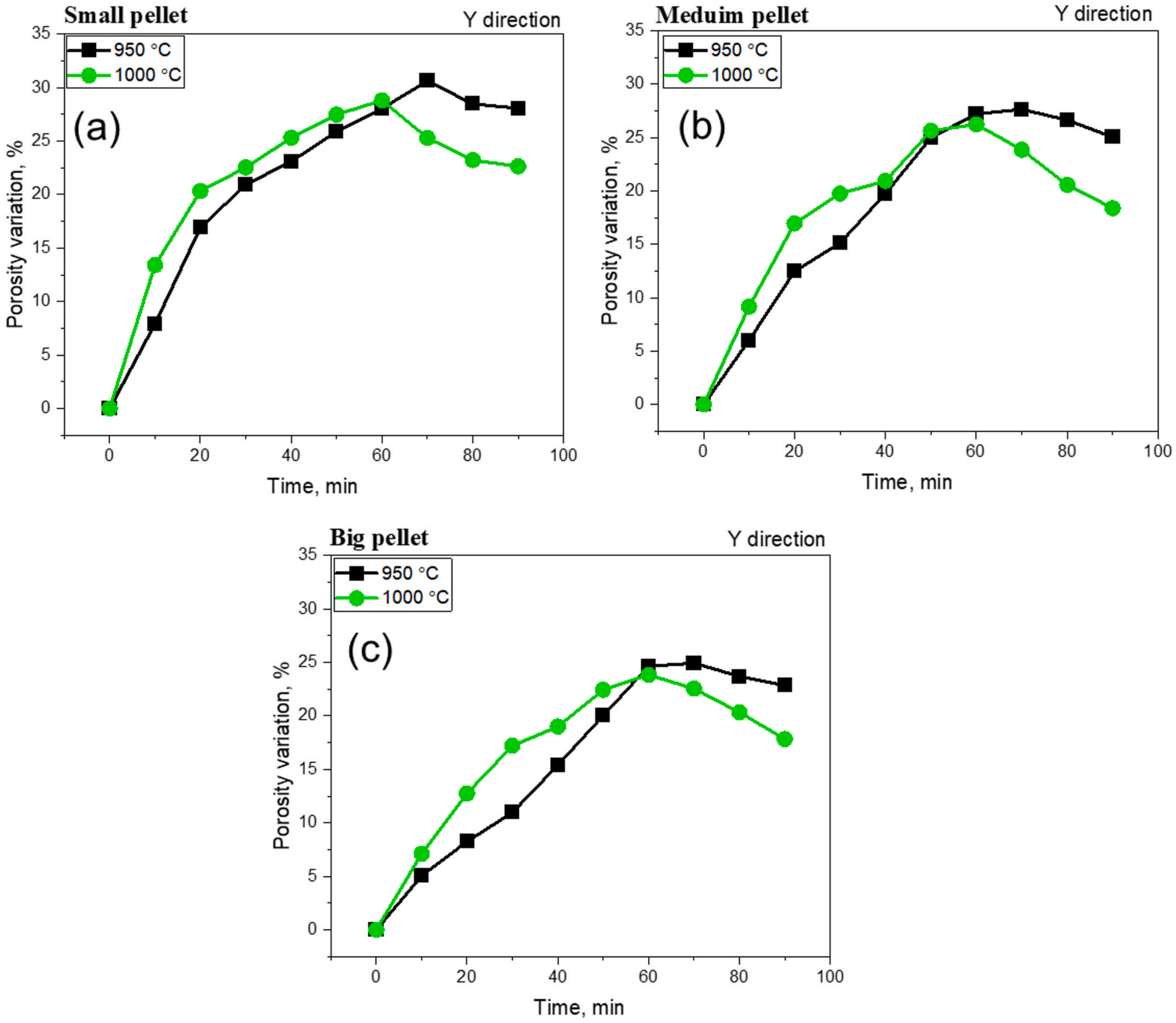

Fig. 22. Comparison between the porosity variation (comes from simulated result) over reduction time at two temperatures of 950 °C and 1000 °C in Y direction for different pellet size (a) small, (b)medium, and (c) big.

of various lattice defects, such as dislocations and cracks. This conclusion is in line of results reported by Kim et al. [1,40]. These changes are an indication of the volume mismatch and the resulting tensions that arise between the reactant and the product phase during the reduction process. This is illustrated by the increased porosity and cracking seen in the accompanying figures, which show the HyDR process at different temperatures and pellet sizes. Obviously, the transformation of W → Fe is accompanied by significant changes in the microstructure of the pellet. In particular, the elastic work required to compensate for the volume changes during the nucleation of Fe acts as an obstacle [1,56], as indicated by the increase in the reduction rate for the W → Fe reaction at the higher temperature of 1000 °C. This increased rate indicates that at this temperature a faster phase transition and consequently a larger volume change takes place, which cannot be completely overcome by elastic deformation of the microstructure of the pellet. When the Fe core forms, the significant volume change associated with this reaction stage and the associated deformation exceed the limits of what can be handled by elastic deformation. In addition, the increase in porosity and cracking as a result of reduction, which is particularly evident in smaller pellets at higher temperatures (1000 °C), leads to a significant reduction in compressive strength as the initial conversion of H to M weakens the structural integrity of the pellet. This is also influenced by pellet size, with larger pellets exhibiting higher strength due to slower reduction kinetics and less pronounced porosity changes [60,61]. The data showing an increased porosity rate, particularly at 1000 °C, is consistent with the concept that the resulting mechanical stresses lead to the formation of cracks as well as creep voids and dislocations within the pellet. These microstructural defects are an expression of the material's attempt to relieve stresses, indicating that the reduction process causes not only chemical changes but also significant mechanical changes.

From a thermodynamic point of view, it should be noted that temperature plays an important role in influencing the reaction pathways and the establishment of equilibrium states during the direct reduction of iron oxide pellets. In the context of iron oxide reduction using pure hydrogen, temperature exerts a decisive influence on the reaction pathways and the equilibrium states, as shown in Table 6. The thermodynamic feasibility of these reactions is determined by the change in Gibbs free energy (ΔG), which is a function of enthalpy change (ΔH), absolute temperature (T) and entropy change (ΔS), according to the equation $\Delta G = \Delta H - T\Delta S$. The reduction reactions proceed via intermediate steps with the ultimate goal of converting iron oxides into elemental iron. For clarification, here are the most important intermediate and total reduction reactions together with their standard changes in Gibbs free energy at 1000 K,

Intermediate reduction reactions [62–65].

(1) $Fe_2O_3 + 3H_2 \rightarrow 2Fe + 3H_2O$	$\Delta G^\circ{}_1 \cong -99$ kJ/mol	(at 1000 K)
(2) $Fe_3O_4 + 4H_2 \rightarrow 3Fe + 4H_2O$	$\Delta G^\circ{}_2 \cong -115$ kJ/mol	(at 1000 K)
(3) $FeO + H_2 \rightarrow Fe + H_2O$	$\Delta G^\circ{}_3 \cong -65$ kJ/mol	(at 1000 K)

Total reduction reaction [64–66].

$Fe_2O_3 + 3H_2 \rightarrow 2Fe + 3H_2O$	$\Delta G^\circ{}_{total} \cong -26.2$ kJ/mol	(at 1000 K)

As the temperature increases, the TΔS term becomes larger, which leads to a more negative ΔG and thus promotes the spontaneous progression of the reduction reactions. Furthermore, it can be deduced that W is thermodynamically more stable compared to H and M at 1000 °C and hydrogen as reducing agent, which is indicated by the relatively less negative ΔG° value for the W reduction reaction. In fact, the higher stability of W at 1000 °C indicates that under a range of conditions where the system does not achieve complete reduction, W is still remained in Fe matrix. This incomplete reduction can lead to a heterogeneous microstructure within the pellet, where regions of unreduced W coexist with reduced iron. This heterogeneity can contribute to an increase in porosity and tortuosity, as can be seen in the previous figures, as the formation of W involves a reduction in volume compared to H and M, creating voids within the pellet matrix. In addition, the presence of different phases with different volumes and thermal expansion coefficients can lead to internal stresses during cooling, potentially causing cracks and further compromising the mechanical integrity of the pellets. The thermodynamic analysis supports our experimental observations and numerical calculations that higher temperatures lead to accelerated reduction kinetics and significant microstructural changes, such as increased porosity. In addition, the bigger pellet size can be expected to contribute to a specific phase composition and different reduction behavior compared to the smaller pellet. The presence and distribution of elements such as silicon, aluminum and calcium in the larger pellet can affect the reaction kinetics and the overall mechanical properties of the pellet.

The initial inhomogeneity seen in the simulated results is consistent with the early stage of porosity development, where porosity increases rapidly, as shown in previous figures. In addition, the observed porosity changes at 950 °C are consistent with the reported slower increase in porosity compared to the faster porosity evolution at 1000 °C. The images document the slower kinetics at the lower temperature, which could lead to a more uniform porosity distribution over time. In the middle stages, the contour patterns indicate enhanced gas transport within the pellet, supporting the notion that increased porosity improves gas-solid interactions. In the later stages, the images show that although porosity increases, the distribution becomes more uneven, indicating potential limitations in the reduction process such as the integrity of the pellet and the onset of sintering. This is important for optimizing the HyDR process to achieve a balance between achieving sufficient porosity for effective reduction and maintaining pellet strength. At a temperature of 1000 °C, the reduction kinetics are primarily driven by temperature, while porosity has a secondary effect. The experimental and simulated results show that the reduction rate and porosity evolution rate are generally higher at 1000 °C than at 950 °C, confirming that higher temperatures enhance the reduction process. This is consistent with the observation that the degree of reduction at the higher temperature of 1000 °C is more influenced by porosity due to the larger surface area and gas-solid interactions associated with higher porosity. Based on the microtomography and the simulated images we provided you with earlier, we were able to determine that the porosity within the pellets is unevenly distributed, which would lead to fluctuations in gas velocity similar to those described above [29].

The presence of larger pores and a complex pore network, as suggested by the higher porosity values in the tables, would create regions of lower resistance where the gas velocity increases. The results also show that the complex pore structure leads to increased flow resistance when gas enters the pores, which is particularly relevant for tortuosity [14,15]. The larger pellets, especially at 1000 °C, exhibit higher porosity evolution rates, indicating an increase in pore complexity and tortuosity. This increased tortuosity acts as a barrier to gas flow, making it more difficult for the gas to penetrate the interior of the pellet and potentially slowing the rate of reduction in the later stages, where tortuosity would have the greatest impact. Finally, the gas velocity in the pores is anisotropic and is influenced by several factors, including pore size and shape [29,39]. At 1000 °C, the porosity rate is significantly increased for all pellet sizes, confirming the assumption that higher temperatures promote faster and more extensive microstructural changes, including greater porosity and lower resistance to gas flow. These changes improve gas-solid interaction due to the greater number of reactive sites and improve the efficiency of the reduction process. The anisotropic gas velocity within the pores [29], which is influenced by the pore size and shape, is also obvious. When the evolution of porosity reaches its peak, we can conclude that the gas velocity increases accordingly in regions of lower resistance, especially near the pellet surface or where larger pores are present. This phenomenon highlights the importance of controlling pellet microstructure and temperature to optimize the direct reduction process, as porosity plays a critical role in facilitating effective gas transport and reaction kinetics. Therefore, the porosity evolution rate is higher at larger pellet sizes and higher temperatures, which means that the gas velocity is higher near the pellet surface and in larger pores. This is consistent with the idea that gas flow favors regions with larger pores and lower resistance, which would also correlate with the SEM images showing larger, more interconnected pores in pellets exposed to higher temperatures.

The present study underlines the need to optimize the direct reduction process in order to improve industrial efficiency and product quality. Based on the experimental and numerical results, a multifaceted approach to optimization is recommended: (1) Careful control of the reduction temperature to balance the kinetics of the reduction with the mechanical stability of the iron pellets, as higher temperatures accelerate the reduction but may compromise the structural integrity due to increased porosity and cracking. (2) Adjusting the size of the iron oxide pellets to control heat transfer and gas diffusion rates, optimize reduction uniformity and minimize thermal stresses. (3) The use of staged reduction strategies, where reduction conditions are adjusted at different stages to favor the formation of specific iron oxide phases, can result in a better controlled microstructure. (4) Continuous monitoring and adjustment of hydrogen flow rates to ensure that the reducing environment is efficiently maintained throughout the process.

Furthermore, the relatively high reaction rates observed with larger iron oxide pellets have significant practical implications for industrial direct reduction processes. Larger pellets, due to their greater porosity and higher reaction rates, are particularly well suited to processes where rapid reduction is the primary concern and where the mechanical integrity of the pellets after reduction is less important. For example, in processes using a multi-stage reduction furnace, larger pellets can be advantageous as they enable faster throughput and greater efficiency in the initial stages of reduction. Furthermore, in processes that involve size reduction after reduction, the fragility caused by the higher porosity of larger pellets can actually be an advantage as it reduces the energy required for subsequent size reduction. However, in processes that require high-strength pellets, such as in a shaft furnace where the pellets are subjected to significant mechanical stress, the size of the pellets must be carefully controlled to prevent structural failure. Therefore, understanding the relationship between particle size and reaction kinetics is crucial for optimizing the iron production process with respect to the specific requirements of the production conditions and the desired product properties.

6. Conclusion

To summaries, the comprehensive analysis of the HyDR process at 950 °C and 1000 °C illustrates the complicated interplay between chemical kinetics, microstructural evolution and mechanical stress in iron oxide pellets of different sizes. Based on the results and discussion, the following conclusions were drawn.

- The data show that higher temperatures accelerate the reduction reactions, especially the transformation of wustite into metallic iron. This phase transition is characterized by a significant volume change that cannot be compensated by elastic deformation alone, leading to the development of lattice defects such as cracks, creep pores and dislocations that serve as stress relief mechanisms.
- The escalated reduction rates and porosity development at 1000 °C as opposed to 950 °C emphasize the central role of temperature in enhancing the kinetics of diffusion and reaction processes. This acceleration promotes greater porosity and pore cross-linking, despite the increased tortuosity, which can act as a barrier to gas flow, unintentionally prolonging the time to complete reduction. Nonetheless, the improved pore structure at elevated temperatures facilitates gas penetration, potentially reducing entropy generation due to mass transfer.
- The microstructural observations emphasize that the porosity in reduced pellets is not only a legacy of the pre-existing conditions, but also a result of the reduction process itself. The increase in free volume and the simultaneous decrease in pore diameter reflect the dynamic nature of the microstructure, which contains additional free volume and defects due to the volume discrepancies and associated stresses between the reactant and product phases.
- The higher porosity evolution rates at higher temperatures and in larger pellets lead to an increase in pore complexity and tortuosity. The increased tortuosity can act as a barrier to gas flow and reduce diffusion and the reduction effect, prolonging the time to reduction. In addition, the higher reduction rates and porosity evolution rates at higher temperatures lead to higher entropy generation due to chemical reactions, but possibly lower entropy generation due to mass transfer as gas penetration improves.
- Ultimately, the results presented show that the total energy input to the HyDR process is a complex balance of factors, including chemical reaction rates, diffusion dynamics and entropy generation. These factors are particularly influential in the initial stages of reduction, where they act as rate-limiting steps. As the process progresses, the driving forces for chemical reactions decrease, resulting in lower entropy generation. This intricate balance determines the efficiency and effectiveness of hydrogen-based direct reduction of iron oxide and is crucial for optimizing the process in industrial applications.

CRediT authorship contribution statement

Behzad Sadeghi: Writing – review & editing, Writing – original draft, Visualization, Project administration, Investigation, Funding acquisition, Formal analysis, Data curation, Conceptualization. **Pasquale Cavaliere:** Validation, Project administration, Funding acquisition, Data curation, Conceptualization. **Mutlucan Bayat:** Software, Methodology, Conceptualization. **Niloofar Ebrahimzadeh Esfahani:** Software, Conceptualization. **Aleksandra Laska:** Visualization, Data curation. **Damian Koszelow:** Visualization, Data curation.

Declaration of competing interest

The authors declare that they have no known competing financial interests or personal relationships that could have appeared to influence the work reported in this paper.

Acknowledgments

The authors would like to thank the Italian Ministry for University and Research (MUR) for the fundings provided under the Grant" green H_2 for clean steels, kinetics and modelling in the direct reduction of iron oxides, decarbonization of hard to abate industry– "real-green-steels", P202278BNF.

Appendix A. Supplementary data

Supplementary data to this article can be found online at https://doi.org/10.1016/j.ijhydene.2024.05.050.

References

[1] Kim S-H, Zhang X, Ma Y, Souza Filho IR, Schweinar K, Angenendt K, et al. Influence of microstructure and atomic-scale chemistry on the direct reduction of iron ore with hydrogen at 700°C. Acta Mater 2021;212:116933.

[2] Ma Y, Filho IRS, Zhang -X, Nandy S, Barriobero-Vila P, Requena G, et al. Hydrogen-based direct reduction of iron oxide at 700°C: heterogeneity at pellet and microstructure scales. Int J Miner Metall Mater 2022;29. 1901.

[3] Wang RR, Zhao YQ, Babich A, Senk D, Fan XY. Hydrogen direct reduction (H-DR) in steel industry—an overview of challenges and opportunities. J Clean Prod 2021; 329:129797.

[4] Raabe D, Tasan CC, Olivetti EA. Strategies for improving the sustainability of structural metals. Nature 2019;575:64–74.

[5] IEA. Global hydrogen review. Paris: IEA; 2022. https://www.iea.org/reports/global-hydrogen-review-2022,License:CCBY4.0. 2022.

[6] Griffin PW, Hammond GP. The prospects for 'green steel' making in a net-zero economy: a UK perspective. Global Transitions 2021;3:72–86.

[7] Agency TIE. The future of hydrogen. Paris: IEA; 2019.

[8] Zakeri A, Coley KS, Tafaghodi L. Hydrogen-based direct reduction of iron oxides: a review on the influence of impurities. Sustainability 2023;15:13047.

[9] Cavaliere P. Hydrogen direct reduced iron. Hydrogen assisted direct reduction of iron oxides. Springer; 2022. p. 233–319.

[10] Cavaliere P, Perrone A, Dijon L, Laska A, Koszelow D. Direct reduction of pellets through hydrogen: experimental and model behaviour. Int J Hydrogen Energy 2023.

[11] Cavaliere P. Hydrogen assisted direct reduction of iron oxides. Springer; 2022.

[12] Xing L, Zou Z-S, Qu Y-x, Shao L, Zou J. Gas–solid reduction behavior of in-flight fine hematite ore particles by hydrogen. Steel Res Int 2018;90.

[13] Battle T, Srivastava U, Kopfle J, Hunter R, McClelland J. Chapter 1.2 - the direct reduction of iron. In: Seetharaman S, editor. Treatise on process Metallurgy. Boston: Elsevier; 2014. p. 89–176.

[14] Cavaliere P, Dijon L, Laska A, Koszelow D. Hydrogen direct reduction and reoxidation behaviour of high-grade pellets. Int J Hydrogen Energy 2023.

[15] Cavaliere P, Perrone A, Marsano D. Effect of reducing atmosphere on the direct reduction of iron oxides pellets. Powder Technol 2023;426:118650.

[16] Ma Y, Souza Filho IR, Bai Y, Schenk J, Patisson F, Beck A, et al. Hierarchical nature of hydrogen-based direct reduction of iron oxides. Scripta Mater 2022;213:114571.

[17] Souza Filho IR, Ma Y, Kulse M, Ponge D, Gault B, Springer H, et al. Sustainable steel through hydrogen plasma reduction of iron ore: process, kinetics, microstructure, chemistry. Acta Mater 2021;213:116971.

[18] Cavaliere PD, Perrone A, Marsano D, Primavera V. Hydrogen-based direct reduction of iron oxides pellets modeling. Steel Res Int 2023;94.

[19] Kazemi M, Pour MS, Sichen D. Experimental and modeling study on reduction of hematite pellets by hydrogen gas. Metall Mater Trans B 2017;48:1114–22.

[20] Piotrowski K, Mondal K, Lorethova H, Stonawski L, Szyma T, Wiltowski T. Effect of gas composition on the kinetics of iron oxide reduction in a hydrogen production process, vol. 30; 2005. p. 1543–54.

[21] Pineau A, Kanari N, Gaballah I. Kinetics of reduction of iron oxides by H_2: Part I: low temperature reduction of hematite. Thermochim Acta 2006;447:89–100.

[22] Parisi DR, Laborde MA. Modeling of counter current moving bed gas-solid reactor used in direct reduction of iron ore. Chem Eng J 2004;104:35–43.

[23] Ranzani da Costa A, Wagner D, Patisson F. Modelling a new, low CO2 emissions, hydrogen steelmaking process. J Clean Prod 2013;46:27–35.

[24] Ajbar A, Alhumaizi K, Soliman M. Modelling and parametric studies of direct reduction reactor. Ironmak Steelmak 2011;38:401–11.

[25] Valipour MS, Hashemi MYM, Saboohi Y. Mathematical modeling of the reaction in an iron ore pellet using a mixture of hydrogen , water vapor , carbon monoxide and carbon dioxide : an isothermal study. Adv Powder Technol 2006;17:277–95.

[26] Nouri S, Ebrahim HA, Jamshidi E. Simulation of direct reduction reactor by the grain model. Chem Eng J 2011;166:704–9.

[27] Bonalde A, Henriquez A, Manrique M. Kinetic analysis of the iron oxide reduction using hydrogen-carbon monoxide mixtures as reducing agent. ISIJ Int 2005;45: 1255–60.

[28] von Bogdandy L, Engell H-J. The reduction of iron ores: scientific basis and technology. Springer Science & Business Media; 2013.

[29] Qiu D, Wang K, Xiong Y, Wei H, Elsherbiny AA, Zhu Y, et al. Numerical simulation on gas behavior inside pellet based on X-ray micro-computed tomography. Powder Technol 2024;433:119270.

[30] Qiu D, Wei S, Elsherbiny AA, Zhang D, Xiong Y, Wei H, et al. Experimental and numerical simulation study on reduction of pellets based on X-ray micro-computed tomography. Metall Mater Trans B 2023;54:3299–311.

[31] Beheshti R, Moosberg-Bustnes J, Kennedy MW, Aune RE. Reduction of commercial hematite pellet in isothermal fixed bed—experiments and numerical modelling. Ironmak Steelmak 2016;43:31–8.

[32] Souza Filho IR, Springer H, Ma Y, Mahajan A, da Silva CC, Kulse M, et al. Green steel at its crossroads: Hybrid hydrogen-based reduction of iron ores. J Clean Prod 2022;340:130805.

[33] Auinger M, Vogel D, Vogel A, Spiegel M, Rohwerder M. A novel laboratory set-up for investigating surface and interface reactions during short term annealing cycles at high temperatures. Rev Sci Instrum 2013;84.

[34] Hjortsberg E, Forsberg F, Gustafsson G, Rutqvist E. X-ray microtomography for characterisation of cracks in iron ore pellets after reduction. Ironmak Steelmak 2013;40:399–406.

[35] Bam LC, Miller JA, Becker M, Basson IJ. X-ray computed tomography: practical evaluation of beam hardening in iron ore samples. Miner Eng 2019;131:206–15.

[36] Cavaliere P, Perrone A, Marsano D. Critical analysis of variable atmosphere gaseous reduction of iron oxides pellets. Ironmak Steelmak 2023;50:1045–64.

[37] Kinaci M, Lichtenegger T, Schneiderbauer S. A CFD-DEM model for the simulation of direct reduction of iron-ore in fluidized beds. Chem Eng Sci 2020;227:115858.

[38] Dong L, Mazzarino I, Alexiadis A. Development of solid–fluid reaction models—a literature review. ChemEngineering 2021;5:36.

[39] Elsherbiny AA, Qiu D, Wang K, Li M, Ahmed M, Hammam A, et al. Parametric study on hematite pellet direct reduction by hydrogen. Powder Technol 2024: 119434.

[40] Ma Y, Souza Filho IR, Bai Y, Schenk J, Patisson F, Beck A, et al. Hierarchical nature of hydrogen-based direct reduction of iron oxides. Scripta Mater 2022;213:114571.

[41] Choisez L, Hemke K, Özgün Ö, Pistidda C, Jeppesen H, Raabe D, et al. Hydrogen-based direct reduction of combusted iron powder: deep pre-oxidation, reduction kinetics and microstructural analysis. Acta Mater 2024;268:119752.

[42] Guo D, Hu M, Pu C, Xiao B, Hu Z, Liu S, et al. Kinetics and mechanisms of direct reduction of iron ore-biomass composite pellets with hydrogen gas. Int J Hydrogen Energy 2015;40:4733–40.

[43] Brännberg Fogelström J. Experimental study of the temperature profile in an iron ore pellet during reduction using hydrogen gas. 2020.

[44] Man Y, Feng JX, Li FJ, Ge Q, Chen YM, Zhou JZ. Influence of temperature and time on reduction behavior in iron ore–coal composite pellets. Powder Technol 2014; 256:361–6.

[45] Shen Z, Sun S, Xu J, Liang Q, Liu H. Experimental and modeling study on reduction and heat transfer characteristics of single iron ore pellet in H_2/CO atmospheres. ISIJ Int 2023;63:42–53.

[46] Dwarapudi S, Ranjan M. Influence of oxide and silicate melt phases on the RDI of iron ore pellets suitable for shaft furnace of direct reduction process. ISIJ Int 2010; 50:1581–9.

[47] Prusti P, Nayak BK, Biswal SK. Study of temperature profile in the induration of magnetite iron ore pellets. Trans Indian Inst Met 2017;70:453–62.

[48] Roque WL, Costa RRA. A plugin for computing the pore/grain network tortuosity of a porous medium from 2D/3D MicroCT image. Applied Computing and Geosciences 2020;5:100019.

[49] He W, Lv W, Dickerson J. Gas transport in solid oxide fuel cells. Springer; 2014.

[50] Welty J, Rorrer GL, Foster DG. Fundamentals of momentum, heat, and mass transfer. John Wiley & Sons; 2020.

[51] Fuller EN, Schettler PD, Giddings JC. New method for prediction of binary gas-phase diffusion coefficients. Ind Eng Chem 1966;58:18–27.

[52] Ghalandari V, Rafsanjani HH. Mathematical modeling and simulation of direct reduction of iron ore in a moving bed reactor by the single particle model. Chemistry & Chemical Technology 2019. 2019;2(13):205–11.

[53] Lara M, Camporredondo J, Garcia A, Castruita L, Equihua F, Moreno H, et al. Thermodynamic simulation of reduction of mixtures of iron ore, siderurgical wastes and coal. Metalurgija 2019;58:11–4.

[54] Jabbour K, El Hassan N. Optimized conditions for reduction of iron (III) oxide into metallic form under hydrogen atmosphere: a thermodynamic approach. Chem Eng Sci 2022;252:117297.

[55] Zheng X, Paul S, Moghimi L, Wang Y, Vilá RA, Zhang F, et al. Correlating chemical reaction and mass transport in hydrogen-based direct reduction of iron oxide. 2023. arXiv preprint arXiv:230214215.

[56] Lin H-y, Chen YW, Li C. The mechanism of reduction of iron oxide by hydrogen. Thermochim Acta 2003;400:61–7.

[57] Devlin A, Kossen J, Goldie-Jones H, Yang A. Global green hydrogen-based steel opportunities surrounding high quality renewable energy and iron ore deposits. Nat Commun 2023;14:2578.

[58] Spreitzer D, Schenk J. Reduction of iron oxides with hydrogen—a review. Steel Res Int 2019;90:1900108.

[59] Zare Ghadi A, Radfar N, Valipour MS, Sohn HY. A review on the modeling of direct reduction of iron oxides in gas-based shaft furnaces. Steel Res Int 2023;94: 2200742.

[60] Metolina P, Ribeiro TR, Guardani R. Hydrogen-based direct reduction of industrial iron ore pellets: statistically designed experiments and computational simulation. Int J Miner Metall Mater 2022;29:1908–21.

[61] Kim G, Pistorius PC. Strength of direct reduced iron following gas-based reduction and carburization. Metall Mater Trans B 2020;51:2628–41.

[62] Kashiwaya Y, Hasegawa M. Thermodynamics of impurities in pure iron obtained by hydrogen reduction. ISIJ Int 2012;52:1513–22.

[63] Turkdogan E. Fundamentals of steelmaking, vol. 656. London: the institute of materials; 1996. p. 96.

[64] Beckers J, van Veldhuizen E, Platier IB, van Minderhout IB. Investigation of the reduction of iron oxide with hydrogen plasma at low sample temperatures. 2018.

[65] Sabat KC, Rajput P, Paramguru R, Bhoi B, Mishra B. Reduction of oxide minerals by hydrogen plasma: an overview. Plasma Chem Plasma Process 2014;34:1–23.

[66] Naseri Seftejani M, Schenk J. Thermodynamic of liquid iron ore reduction by hydrogen thermal plasma. Metals 2018;8:1051.